Effect of surface hydraulics and salmon redd size on redd induced hyporheic exchange

Bishal Bhattarai[1], Brandon Hilliard[2], William J. Reeder[2], Ralph Budwig[2], Benjamin T. Martin[3], Tao Xing[1*] and Daniele Tonina[2]

1. Department of Mechanical Engineering, University of Idaho, Idaho, USA
2. Center for Ecohydraulics Research, University of Idaho, Idaho, USA
3. Institute for Biodiversity and Ecosystem Dynamics, University of Amsterdam, Amsterdam, the Netherlands

*Corresponding Author

ABSTRACT

Salmonids bury their eggs in hyporheic streambed gravel, forming an egg nest, called a redd, characterized by a pit and a hump topography resembling a dune. Embryos' survival depends on downwelling oxygen-rich stream water fluxes, whose magnitudes are expected to depend on the interactions among redd shape, stream hydraulics, and the hydraulic conductivity of the streambed sediment. Here, we hypothesize that downwelling fluxes increase with stream discharge and redd aspect ratio, and such fluxes can be predicted using a set of dimensionless numbers, which include the stream flow Reynolds and Froude numbers, the redd aspect ratio, and the redd relative submergence. We address our goal by simulating the surface and subsurface flows with numerical hydraulic models linked through the near-bed pressure distribution quantified with a two-phase (air-water) two-dimensional surface water computational fluid dynamics model, validated with flume experiments. We apply the modeling approach to three redd sizes, which span the observed range in the field (from ~1 to ~4 m long), and by increasing discharge from shallow (0.1 m) and slow (0.15 m/s) to deep (8m) and fast (3.3 m/s). Results support our hypothesis of downwelling fluxes increasing

with discharge and redd aspect ratio due to the increased near-bed head gradient over the redd. The derived equation may help evaluate the effect of regulated flow (e.g., hydroelectric and flood control dams) on redd-induced hyporheic flows.

Keywords:

hyporheic zone, salmon redd, flow discharge, downwelling flows

Key statements:

(1) Redd-induced hyporheic exchange increases with discharge and redd aspect ratio

(2) Hyporheic downwelling flows are a function of surface Reynolds and Froude numbers and redd aspect ratio

(3) Disturbed material hydraulic conductivity can be used to predict the downwelling flux instead of categorical heterogeneity for the sediments

1 INTRODUCTION

Salmon females bury their eggs in streambed gravel, forming an egg nest (Crisp & Carling, 1989; Deverall et al., 1993) having a typical dune-like shape (Figure 1). These dune-like features are commonly referred to as a redd. To construct a redd the female excavates a hole, where she lays her eggs, by redirecting the surface flow with her tail (Burner, 1951; Chapman, 1988; Groot & Margolis, 1991). These egg pockets can range from 15 to 50 cm in depth, depending on fish size, species, and hydromorphological conditions (DeVries, 1997). After the eggs are fertilized by a salmon male, female salmons cover them (forming the hump, Figure 1) with the sediment moved by digging a new hole (forming the pit, Figure 1). This spawning activity results in a characteristic redd shape of a pit followed by a hump, called the tailspill (Figure 1) (Bjornn & Reiser, 1991), which has a higher permeability than the undisturbed sediments due to the winnowing away of fine grains and loosening of the sediment matrix (Coble, 1961; Merz et al., 2004; Tappel & Bjornn, 1983; Zimmermann & Lapointe, 2005a). This shape resembles a dune, with an amplitude, A, equal to the difference in elevation between the bottom of the pit and the top of the tailspill, and its length, L, equal to the distance between the beginning of the pit and the end of the tailspill (Figure 1) (Crisp & Carling, 1989; DeVries, 1997).

Salmonids may repeat their spawning activities several times resulting in more than one egg pocket in a single redd. In other cases, several spawners may use the same area to form superimposed redds (Hendry et al., 2004). Thus redd size may vary not only due to flow velocity and depth, excavating fish size, and sediment size (DeVries, 1997; Riebe et al., 2014), but also due to multiple spawning activities in the same location. This results in a potentially wide range of redd sizes from small redds of a few centimeters in amplitude and nearly 1 m long (e.g., sockeye salmon (*Oncorhynchus nerka*) (Hassan et al., 2015)) to large redds of decimeter amplitude and multiple meters in length (e.g., Chinook salmon (*Oncorhynchus tshawytscha*) (Bjornn & Reiser, 1991; DeVries, 1997, 2012; Evenson, 2001; Tonina & Buffington, 2009a)). This size range may cause different hydrodynamic properties of the redd because of different aspect ratios, A_R (= A/L) (Buxton, Buffington, Yager, et al., 2015), and different amplitudes protruding into the freestream flow.

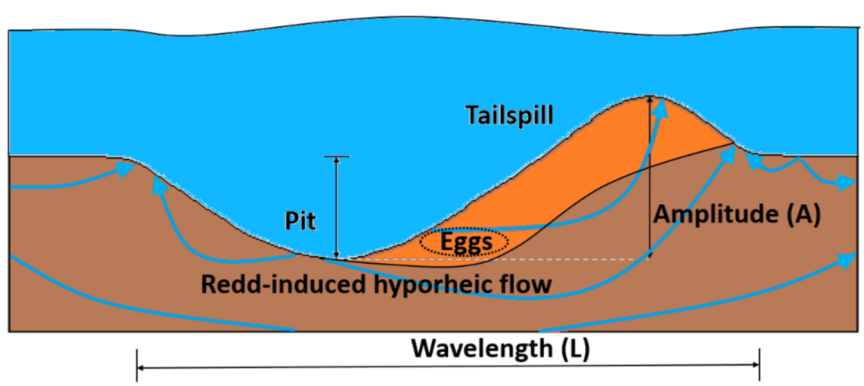

Figure 1: Sketch of a longitudinal profile of a redd along the plane intersecting the center of the redd with expected hyporheic flow lines (modified from Tonina and Buffington (2009a)). Orange color indicates streambed material disturbed during spawning activity with higher hydraulic conductivity (K_D) than the undisturbed streambed (brown) material (K_{UD}).

Soon after spawning, the female salmon dies, while her embryos develop within the gravel over several weeks (Bjornn & Reiser, 1991; Boyd et al., 2010). Their successful development depends on hydrological and chemical characteristics within the redd (Bjornn & Reiser, 1991; Martin et al., 2017), whose organic environment is supported by oxygen-rich stream waters entering, flowing through, and exiting the streambed sediment (Coble, 1961; Cooper, 1965; Stuart, 1953b). This water exchange is known as hyporheic exchange (Boano et al., 2014; Tonina & Buffington, 2009b) and stems from the interaction between the freestream flow and the redd, causing large hydraulic head gradients over upstream side of the tailspill, where stream water is driven into the sediment towards the egg pocket (Figure 1), and low hydraulic heads near the tailspill crest, where hyporheic water upwells back into the stream flow (Cardenas et al., 2016; Cooper, 1965; Stuart, 1953a) (Figure 1). This redd-induced hyporheic exchange is shallower than and superimposed over hyporheic exchange caused by large-scale streambed topography, like a pool and riffle (Tonina & Buffington, 2009a). This exchange is assumed to be discharge-dependent (Cardenas et al., 2016), but as discharge increases, both flow velocity and depth increase and their relative importance on redd-induced hyporheic flows is not well understood. Since the redd morphology resembles a dune, Buxton et al. (2015), recently modeled hyporheic flow through dunes using the equation of Elliot and Brooks (Elliott, 1990; 1997b, 1997a) which were derived from Fehlman's (1985) experiments for dune-like bedforms. The Elliot and Brooks equation suggests an increase in pressure difference - and thus hyporheic exchange - with an increase in velocity but a decrease with increasing water depth. Both pressure and velocity increase with an increasing discharge, but their relative increase depend on riverine morphology. Furthermore, Fehlman's (1985) experiments had two similar dune sizes and very narrow ranges of flow velocities and depths. In contrast, besides having broad size ranges and aspect ratios, redd locations may experience shallow (a few centimeters) and deep (several meters) mean flow depths with slow (a few centimeters per second) and fast (a few meters per second) mean flow velocities. Consequently, the hydrological and morphological conditions of salmon redds go beyond those modeled by Fehlman's (1985) experiments. Thus, the equation proposed by Elliot and Brooks (Elliott, 1990; 1997a) may not be appropriate in predicting hyporheic exchange within redds under flow scenarios different from the shallow and slow freestream velocities used in the experiments.

This is an important limitation in predicting the impact of regulated flows (reservoir management or water extraction) on embryo survival because of their dependence on downwelling velocities (Coble, 1961; Martin et al., 2020). Many salmonid species may spawn in river reaches downstream of reservoirs, whose operations control stream discharge rather than headwater streams (Geist & Dauble, 1998; Yates et al., 2008). However, information on the impact of such management on redd habitat is limited especially during drought years when water flow is curtailed.

We aim to address this knowledge gap and study the impact of redd size and surface hydraulics on hyporheic flows within redds and the near-bed pressure gradient over redds. Based on previous evidence (Cardenas et al., 2016; Fehlman, 1985; Tonina & Buffington, 2009a), we hypothesize that downwelling fluxes increase with stream discharge and redd aspect ratio, and they can be predicted from a set of dimensionless numbers, including the freestream flow Reynolds and Froude numbers, the redd aspect ratio, and the redd relative submergence. We also investigate the effect of heterogeneous (dual) hydraulic conductivities between disturbed (within the redd) and undisturbed (surrounding streambed) sediments on hyporheic fluxes. We address our goal by simulating surface and subsurface flows with two-dimensional numerical hydraulic models linked through the near-bed pressure distribution quantified with a two-phase (air-water) surface water computational fluid dynamics model. We applied the modeling approach to five redd sizes with L, M, S, VS and ES identifying the large, medium, small, very small and extremely small, which span the observed range in the field (from ~1 to ~4 m long) (Bjornn & Reiser, 1991; DeVries, 1997, 2012; Evenson, 2001;

Tonina & Buffington, 2009a) and imposed stream discharges spanning from shallow (0.1 m) and slow (0.15 m/s) to deep (8 m) and fast (3.3 m/s) waters. The paired depth-velocity values were selected from those observed near redd locations along the Sacramento River (California, USA) downstream of the Shasta dam. Results support our hypothesis of downwelling fluxes increasing with discharge or redd aspect ratio due to an increase in the near-bed head gradient over the redd.

2 METHODS

We used a two-dimensional (2D) computational fluid dynamics (CFD) model (ANSYS®) to simulate surface (Reynolds averaged Navier Stokes equation, RANS) and groundwater (Darcian flow) hydraulics numerically. The two domains were simulated separately and linked via the near-bed pressure distribution (Janssen et al., 2012) induced by 2D simplified salmon redds (Cardenas et al., 2016), whose dimensions span those found in the literature. The surface model was validated by comparing CFD results with laboratory measurements of near-bed pressures from Fehlman (1985) as done by others (Cardenas & Wilson, 2007; Reeder et al., 2018; Trauth et al., 2013) and by data from experiments in our salmon redd physical model. The results from the surface and subsurface models were interpreted with a set of dimensional numbers to generalize the results for the pressure drop around the redd and the interstitial downwelling fluxes through the redd (Monofy & Boano, 2021).

2.1 Surface flow hydraulics

Open flow surface hydraulics were modeled by solving the RANS equations with a κ-ε realizable turbulence closure scheme incorporated within the finite volume ANSYS software program. This turbulence closure was chosen because of its higher performance over other schemes in terms of predicting flows with strong streamlines curvature, flow separations and flows with complex secondary flow features (*ANSYS Fluent Theory Guide*, 2019). Surface water elevation of open channel flows with the fixed lid approach (Janssen et al., 2012), which prescribes the water surface elevation with an impermeable, slip, and no-shear wall condition, may not properly capture the spatial gradients that are present in open flows (Meselhe & Odgaard, 1998; Monsalve & Yager, 2017). As a result, we treated the system as a two-phase (air and water) problem and tracked the water surface elevation at the air-water interface using the volume of fluid (VOF) approach (Hirt & Nichols, 1981). The water surface profile was extracted at locations where the volume fraction is 0.5, where values of 1 or 0 represent only water or air, respectively. We used a long flow domain with two fixed-lid sections upstream and downstream of a 45 m long two-phase domain to train and develop the flow (Figure 2a). We ran all simulations for at least two flow cycles throughout the full domain to ensure that the flows were in equilibrium with the boundary conditions. The water-sediment interface was specified as a no-slip impermeable boundary, which is a typical condition for this problem (Cardenas & Wilson, 2007b; Chen et al., 2015), because momentum and mass exchanges with porous sediment are small and have negligible influence on surface hydraulics (Janssen et al., 2012). Water boundaries were defined as velocity inlet and velocity outlet conditions for the upstream and downstream locations respectively, whereas air boundaries were specified as pressure outlets. The entire domain was sloped to resemble a streambed gravity flow (Elliott & Brooks, 1997b; Fehlman, 1985). There are approximately two million quadrilateral cells with a mean cell size of about 2.4 cm in the horizontal direction. We employed a highly refined 1.5 mm cell size in the vertical direction at the air-water interface to accurately track water surface elevation and a very small vertical cell size of about 0.1 mm near the bottom boundary (Figure 2b). We ran mesh independence tests with three different mesh sizes (fine, medium, and coarse) by reducing the mesh dimensions by 30%, and compared their predicted pressure distributions, which resulted in a change of total head drop through the redd of less than 3% from the fine to coarse mesh. Therefore, all simulations were conducted with the medium mesh to save computational cost.

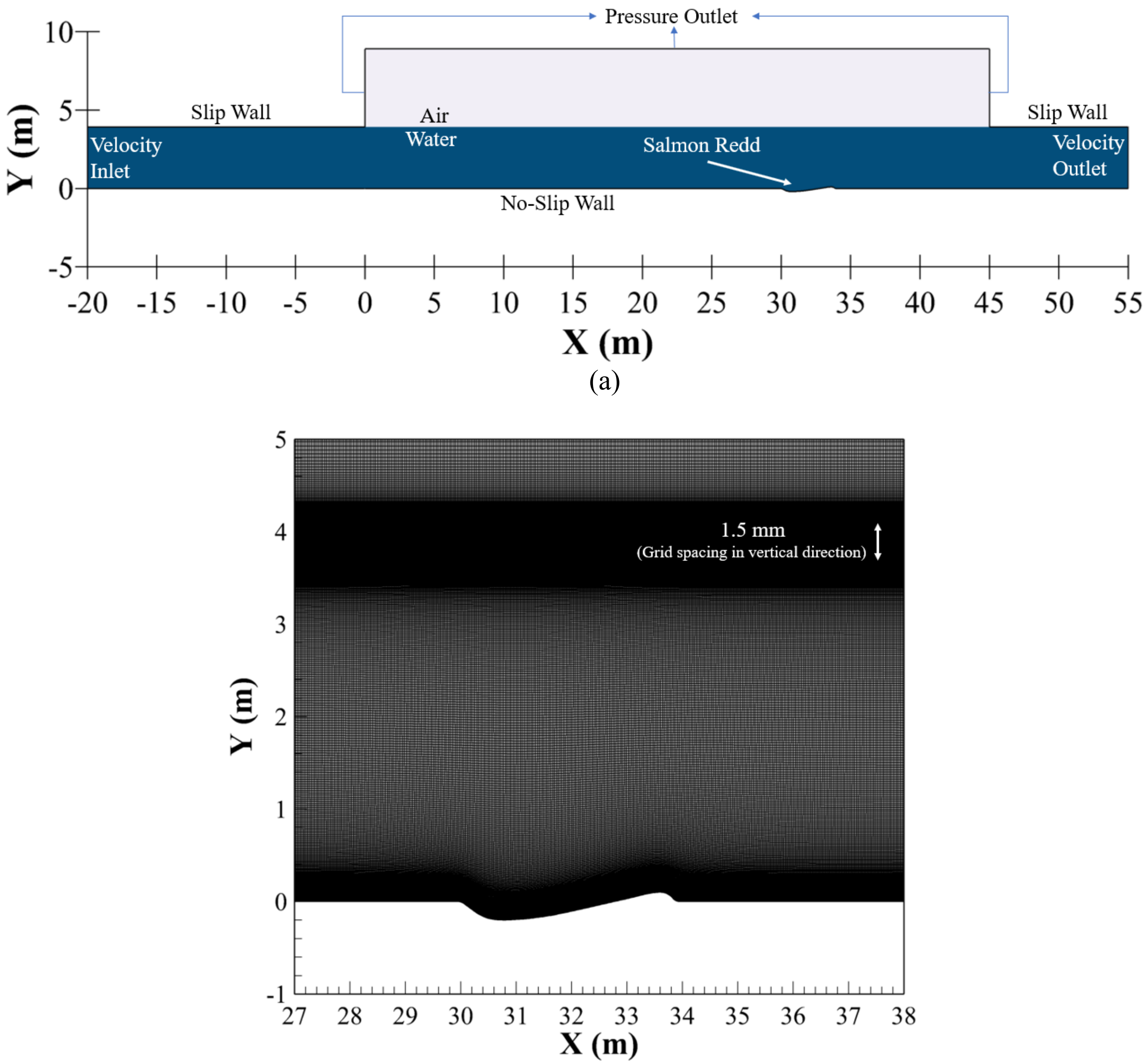

Figure 2: Simulation domain design: (a) surface flow domain with air colored in grey and water colored in blue along with the boundary conditions, and (b) Zoomed-in section near the redd showing the mesh.

2.2 Groundwater flow hydraulics

A steady-state Darcian groundwater flow was solved to predict the redd-induced interstitial flows (Cardenas et al., 2016; Tonina & Buffington, 2009a) in ANSYS. The water-sediment interface was defined as a pressure inlet boundary with the specified pressure distribution predicted from the CFD surface model. A periodic boundary condition, which simulates an infinite periodic domain, was applied at the upstream and downstream locations of the subsurface domain boundaries with an ambient groundwater flow of nearly 0.001 mm/s, which mimics a large-scale longitudinal groundwater underflow caused by a valley slope. The bottom boundary was treated as a no-slip impermeable wall positioned five meters below the flat water-sediment interface to not affect the redd-induced hyporheic flow. The average grid cell size was 2.5 cm horizontally and 1.5 cm vertically, resulting in approximately one million quadrilateral cells. The permeability, k, was set to be homogenous and isotropic, with a value of $5.1 \cdot 10^{-11}$ m^2, equivalent to a hydraulic conductivity of $K = 0.0005$ m/s.

Due to the winnowing of fine material and loosening of the sediment matrix during the redd construction, newly formed redds have a higher hydraulic conductivity, K_D (disturbed sediment), than that of the undisturbed streambed material, K_{UD} (undisturbed sediment). These two different hydraulic conductivities form a categorical heterogeneous system, which may result in higher mean downwelling flow than the homogenous case. To investigate this possibility, we studied a case of categorical heterogeneity for run 14, M (Table 4), a medium redd with surface flow depth of 3.92 m and velocity of 1.49 m/s. The hydraulic conductivity within the redd, ($K_D = 5 \cdot K_{UD}$ and $10 \cdot K_{UD}$) was increased by half an order of magnitude and one full order of magnitude as documented in the literature (Zimmermann & Lapointe, 2005a) from that of the surrounding undisturbed sediment ($K_{UD} = K = 0.0005$ m/s) (Figure 1). Because hyporheic flow is chiefly a near-surface process, we hypothesized that the hydraulic conductivity of the redd would dominate the redd-induced hyporheic flows and thus the effect of categorical heterogeneity between the disturbed and undisturbed sediment would be negligible, causing the system to be treated as homogenous with the hydraulic conductivity of the redd as the reference property. This heterogeneity is different from the internal heterogeneity caused by the redd internal architecture which may form zones of progressive lower hydraulic conductivity from the egg pocket to the redd surface (Chapman, 1988).

3 CFD SIMULATIONS VERIFICATION AND VALIDATION

We validated the CFD modeling by comparing flow hydraulics predicted by the model with those measured in the flume experiments with dune bedforms conducted by Fehlman (1985) as well as those of a redd bedform conducted by us in this study. We also quantified uncertainty due to measurement errors and validated the mesh and time-step used in the simulations.

3.1 Fehlman's (1985) flume experiments

Redds have similar geometry to dunes, so we used Fehlman's (1985) data set which contains pressure distributions over dunes to validate the CFD modeling. We selected two experiments that have the same average flow depth of 0.22 m but two distinct average flow velocities of 0.29 m/s and 0.44 m/s (Fehlman, 1985). We simulated the entire flume experiment as an open channel flow and extracted the pressure and water surface profiles at the 8^{th} (center) dune, out of 15 consecutive dunes as done experimentally by Fehlman (1985). Simulation performance was quantified with Nash-Sutcliffe coefficients (NSC) whose values indicate the quality of the model performance: very good ($NSC > 0.75$), good ($0.65 < NSC \leq 0.75$), satisfactory ($0.5 < NSC \leq 0.65$), and unsatisfactory ($NSC \leq 0.5$) (Moriasi et al., 2007). The accuracy of the comparison by visual inspection between predicted and measured pressure distributions (Figure 3a) is comparable to that reported in the literature (Cardenas et al., 2016; Reeder et al., 2018). The NSC of 0.7 and 0.6 for flows with velocity 0.29 m/s and 0.44 m/s respectively also support the visual inspection. Unlike previous studies, we also modeled the respective water surface elevations to those reported by Fehlman (1985) with NSC values of 0.8 and 0.7 (Figure 3b).

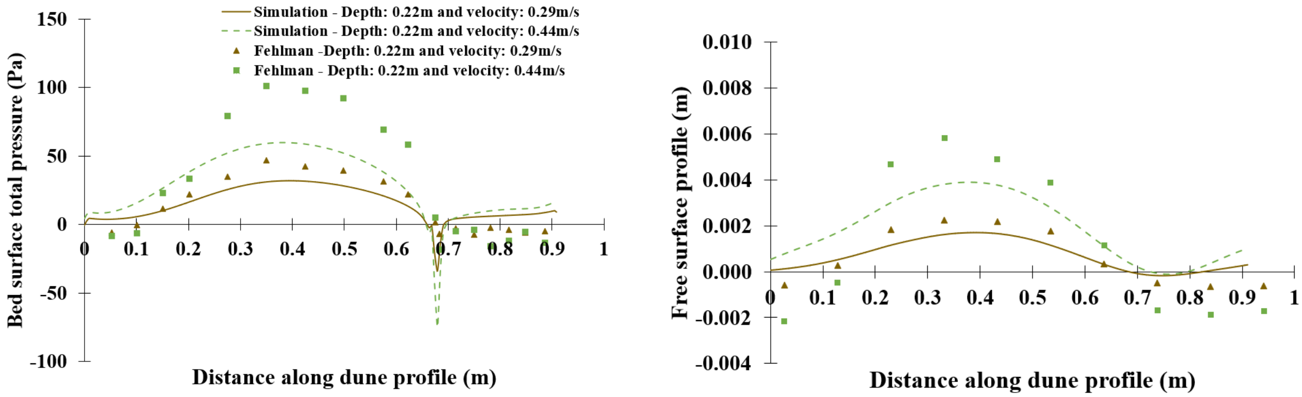

(a) (b)

Figure 3*:* Comparison between simulations (lines) and Fehlman's experiments (symbols) for (a) total pressure and (b) free surface profiles at the 8th dune.

3.2 Redd experiments

We conducted four experimental runs with four combinations of upstream flows: two depths of shallow (0.1 m) and deep (0.2 m) water and two velocities of slow (0.1 m/s) and fast (0.2 m/s) flow in a 7 m long, 0.5 m wide, and 0.7 m deep recirculating flume (Table 1) at the Center for Ecohydraulics Research (Bhattarai et al., 2022; Moreto et al., 2022). The redd, which was a ¼-scaled version of an average redd was made with THV grains which are on the order of 3 mm in nominal diameter. The rest of the sediment was made with crashed glass of about 3 mm in size. The redd was placed in the middle section of the flume to minimize boundary effects. The water passed through a flow straightener before entering the flume while a weir gate regulated the downstream boundary. Stereo Particles Image Velocimetry, or SPIV, was used to map the flow field downstream of the redd crest where complex hydraulics occur to validate the CFD model. We collected the flow field from the upstream at x = -1.14 m and the downstream at x = 1.42 m to define boundary conditions for the streamwise (Vx) and vertical (Vy) velocities (Vy was less than 2% of Vx) and turbulence kinetic energy (TKE) profiles for the CFD models (Figure 4a). 2,000 image pairs were collected during the SPIV experiments, which ensured ergodicity of the flow field (Moreto et al., 2022).

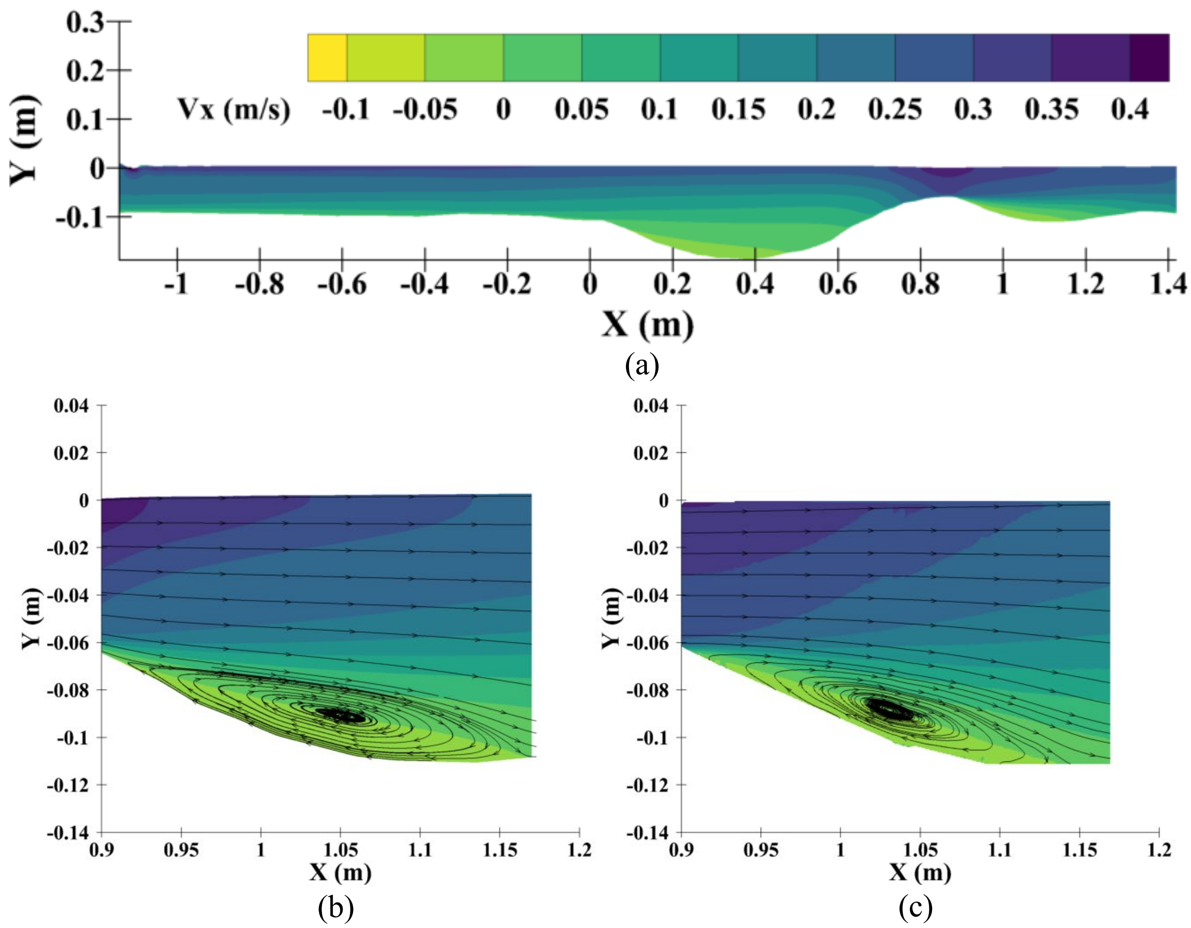

Figure 4: Velocity field for the shallow-fast case for (a) the entire simulation domain and (b) close-up views downstream of the redd crest simulated by CFD and (c) measured with stereo particle image velocimetry.

Table 1. Four experimental flow conditions used as CFD boundary conditions, with average depths (averaged between the upstream and downstream), average velocities, and average TKE.

Runs Description	**Avg Depth (m)**	**Avg velocity (Vx) (m/s)**		**Avg TKE (m^2/s^2) $\times 10^{-4}$**	
		Upstream	**Downstream**	**Upstream**	**Downstream**
Shallow-fast	0.105	0.191	0.209	2.13	20.4
Shallow-slow	0.098	0.103	0.109	0.638	6.18
Deep-fast	0.1974	0.175	0.169	0.933	4.77
Deep-slow	0.1972	0.085	0.081	0.194	1.26

Comparisons of the overall size of the separation vortex and reattachment locations show very good agreement between the measured and CFD predicted flow fields downstream of the redd (Figure 4b and Figure 4c). Comparisons between x-velocity profiles just downstream of the crest (x = 0.95 m) and near the bottom of the hump (1.15 m) for all four flow cases give very good NSC values of 0.954

and 0.969 for the shallow-fast flow, 0.824 and 0.967 for shallow-slow flow, 0.644 and 0.923 for deep-fast flow, and 0.6 and 0.845 for deep-slow flow at x = 0.95 m and x = 1.15 m, respectively (Figure 5). This confirms that our CFD model adequately predicted the flow field caused by the redd-flow interaction.

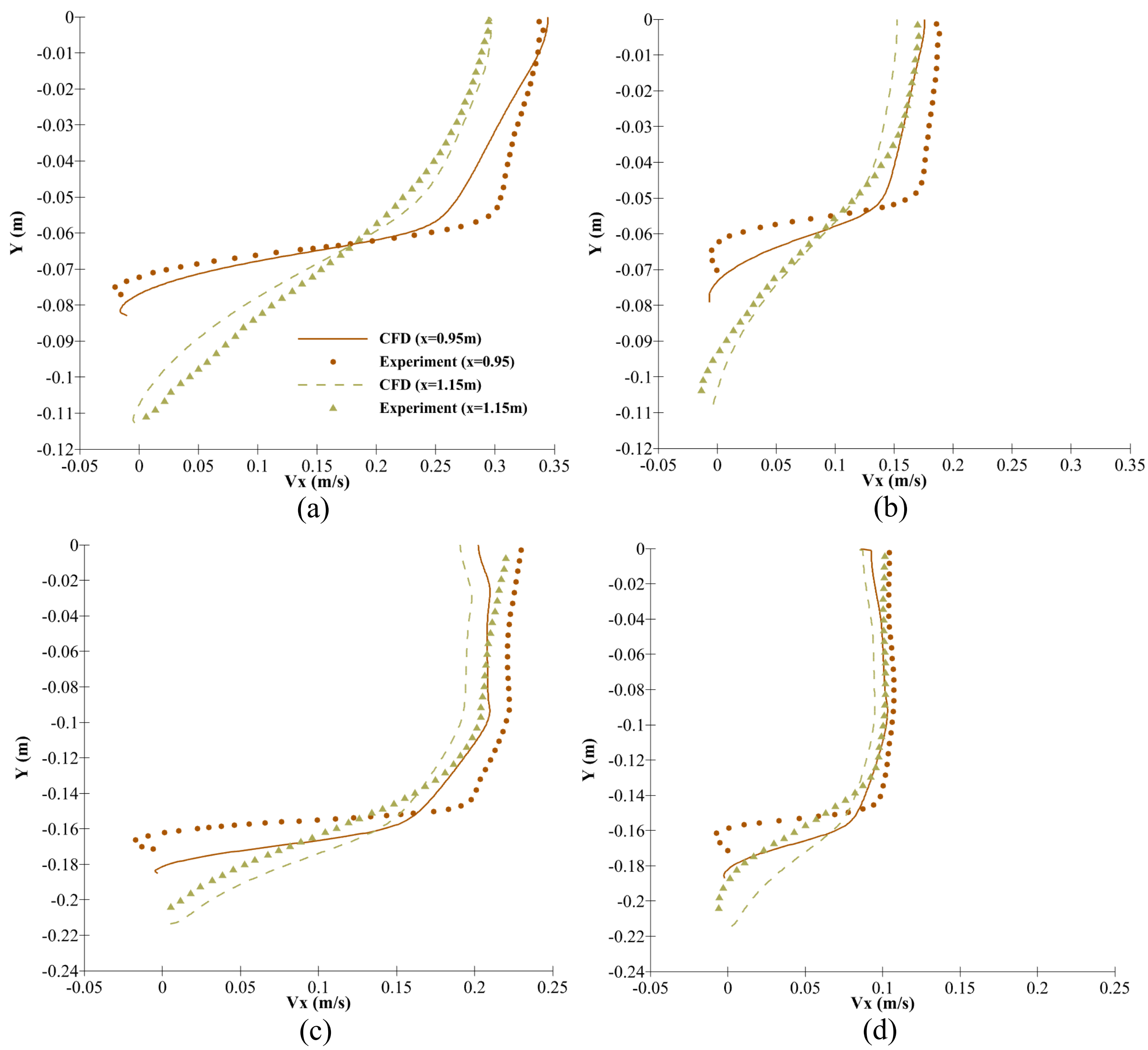

Figure 5: Comparison between the simulated (solid and dash) and experimental (symbols) x-velocity profiles at x = 0.95 m and 1.15 m for (a) shallow-fast, (b) shallow-slow, (c) deep-fast, and (d) deep-slow flows.

3.3 Mesh size, time-step resolution, and flow uncertainty validation

To ensure that the results are independent of mesh and time-step resolutions, we performed a solution verification for Vx on three systematically refined meshes (fine, medium, and coarse) for the shallow-fast flow case, which is the most critical one. The overall grid size, total number of grid points, and time step size used are given in Table 2. We used a grid refinement ratio, $r_G = {}^{\Delta x_2}/_{\Delta x_1} = {}^{\Delta x_3}/_{\Delta x_2}$=1.414, where Δx is the grid distance between two elements and the subscripts 1, 2, and 3 represent the fine, medium, and coarse meshes, respectively. The overall procedure is as described in (Xing et al., 2008; Xing & Stern, 2010, 2011). The convergence ratio, denoted by R_G, is the ratio of solution differences for medium-fine and coarse-medium solution pairs. L2 norms of x-velocity profiles are used to calculate $\varepsilon_{G_{21}}$ and $\varepsilon_{G_{32}}$ to define the ratios for R_G and P_G (observed order of accuracy), i.e.,

$$\langle R_G \rangle = \left\| \varepsilon_{G_{21}} \right\|_2 / \left\| \varepsilon_{G_{32}} \right\|_2 \tag{1}$$

$$\text{where } \left\| \varepsilon_{G_{21}} \right\|_2 = \sqrt{\textstyle\sum_{k=1}^{N} (P_1 - P_2)^2} \tag{2}$$

$$\langle P_G \rangle = \frac{ln(\left\| \varepsilon_{G_{32}} \right\|_2 / \left\| \varepsilon_{G_{21}} \right\|_2)}{\ln{(r_G)}} \tag{3}$$

where $\langle\ \rangle$ & and $\|\ \|_2$ denotes a profile-averaged quantity (solution change ratio based on L2 norms) and L2 norm, respectively (Wilson et al., 2001). N is the number of points along a single velocity profile and P_1 and P_2 are the point solutions (Vx) for meshes 1 and 2, respectively. U_G is the numerical uncertainty estimate and $|E|$ is the absolute relative error between the fine mesh and the experimental data, representing a measure of bias error between the numerical and experimental results ($|E| = |S - D|$), where S is the fine mesh streamwise average velocity, and D is the experimental streamwise average velocity. U_V is the validation uncertainty ($U_V = \sqrt{U_G^2 + U_D^2}$), where U_D is the experimental uncertainty, representing an average uncertainty of the numerical and experimental results. Validation is achieved when $|E| < U_V$.

Table 2. Solution verification.

Grids	Grid Dimensions	Total Number of Points	Time step size
1	869 × 220	191,180	0.002
2	615 × 155	95,325	0.002828
3	430 × 108	46,440	0.004

For the solution verification and validation study, we used four locations (x = 1 m, 1.05 m, 1.1 m, and 1.15 m). The grid triplet showed monotonic convergence ($0 < R_G < 1$) at all horizontal locations with small grid uncertainty values ranging from 31.7 %D to 62.5 %D. All four locations showed that the model was validated ($|E| < U_V$) in (Table 3).

Table 3. Verification & Validation study for the longitudinal component of the velocity. Percentages are calculated using experimental data (%D).

x-location (m)	R_G	P_G	U_G	U_G (%D)	U_D (%D)	|E| (%D)	U_V (%D)
1.0	0.23	2.07	0.0695	31.69	0.33	1.36	31.7
1.05	0.24	2.05	0.0638	32.68	0.41	2.56	32.68
1.1	0.27	1.87	0.066	36.17	0.5	3.57	36.17
1.15	0.39	1.36	0.11	62.53	0.55	2.70	62.53

4 FLOW SCENARIOS

We developed a set of 32 flow simulations using paired mean flow depth and velocity values obtained at redd locations along the Sacramento River for Chinook salmon (*Oncorhynchus tshawytscha*) (Table 4) (Data from NOAA, Andrew Pike, Winter-run Chinook salmon Lifecycle model project, see data repository). The Sacramento River data (19 velocity-depth sets) were augmented with one set of surface water information from the Columbia River (Mueller, 2005), six sets of Fehlman's (1985) flume experimental runs, two sets from Deverall's (1993) field data, and four additional depth-velocity sets to increase the range to shallower flow conditions than those observed in the data of the Sacramento River. We used three redd sizes to account for their natural variation: large, medium, and small, with lengths of 3.9, 2.8, and 1.82 m and aspect ratios of 0.077, 0.139, and 0.265, respectively (Deverall et al., 1993; Evenson, 2001; Tonina & Buffington, 2009a). These three sizes were augmented with two additional smaller redd sizes for shallow water conditions to mimic egg nests built by salmonids, such as sockeye salmon (*Oncorhynchus nerka*) smaller than Chinook salmon. The smaller redds had wavelengths of 1.0 m and 0.914 m, with aspect ratios of 0.139 and 0.15, respectively.

5 DATA ANALYSIS

We expressed pressure (P) as pressure head with a unit of meters of water, i.e., P/γ, where γ is the specific weight of water. To compare the distributions among all scenarios, we removed the effect of the hydrostatic pressure over the undisturbed inclined bed and the local slope by defining the relative total head, $H_R = H-(Y_0+z)$, where H is the total head, Y_0 is the undisturbed hydraulic depth away from the redd based on the inlet water depth and z is the difference between the local streambed and the datum that are sloped at the same angle (Figure 6). This is similar to Fehlman's (1985) approach, but while he referenced the pressure to the depth at the dune crest, we used Y_0 and mean flow velocity, u, upstream enough from the redd as a reference value. These values would be similar to those quantified at the reach scale which would be available through one-dimensional hydraulic modeling or discharge field surveys. The use of H_R eliminates the influence of the large static pressure (Y_0) running over small near-bed pressure variations and mean streambed slope for all simulations, allowing visualization of the pressure difference from its mean value. This pressure gradient induces the hyporheic exchange (Elliott & Brooks, 1997b) (Figure 1). The relative water surface elevation (WSE_R) is defined as the difference between the local free surface elevation and the undisturbed free surface elevation based on water depth at inlet (Figure 6).

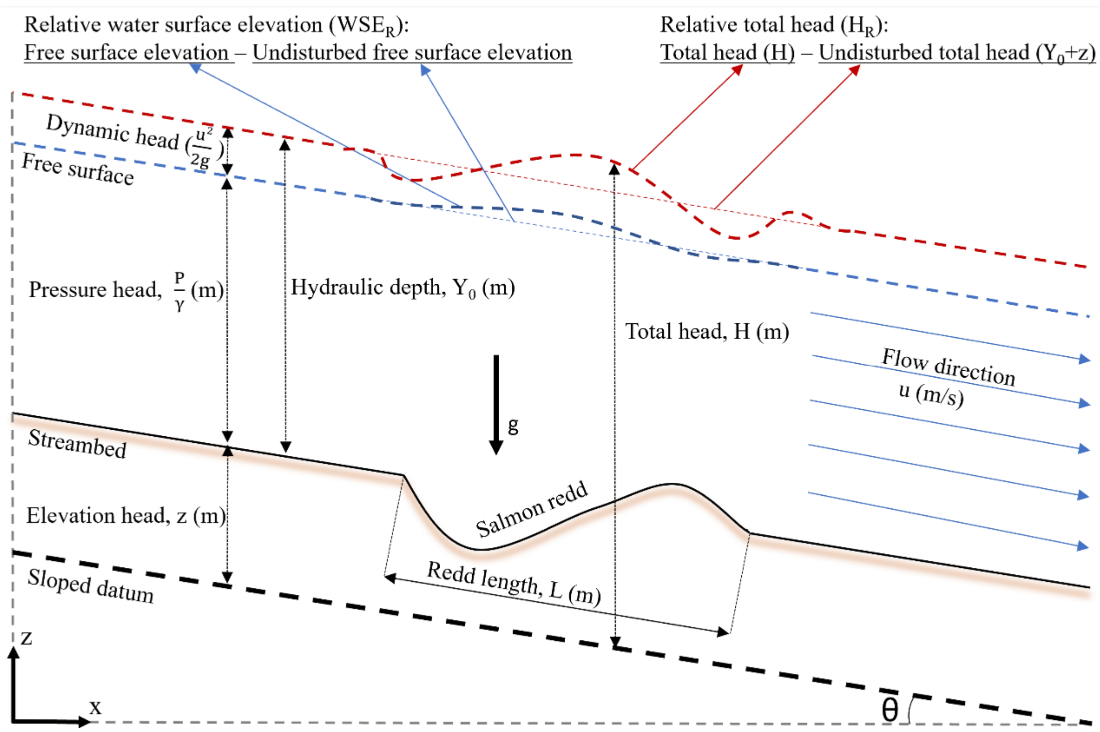

Figure 6: An illustration of all heads flowing across the redd in an open channel flow (the slope angle is so small such that the water depths in the vertical direction z and normal direction of the slope are functionally identical).

6 Dimensional Analysis

From a dimensional analysis of the problem, we found that the redd-induced total head drop, $\Delta H_R = H_{R,H} - H_{R,L}$, with $H_{R,H}$ and $H_{R,L}$ being the maximum and minimum relative total heads over the redd, respectively, depends on seven quantities: mean cross-sectional velocity, u, undisturbed hydraulic depth, Y_0, gravity, g, dynamic viscosity, μ, the density of water, ρ, redd amplitude, A, and redd length, L. The application of the Buckingham theorem reduces them to a set of five dimensionless groups, which are the pressure gradient, $H^* = \frac{\Delta H_R}{L}$, the redd aspect ratio, A_R, the redd relative submergence, A/Y_0, freestream Reynolds number, $Re = \frac{u \cdot Yo}{\nu}$ and the freestream Froude number, $Fr = \frac{u}{\sqrt{g \cdot Yo}}$. A similar analysis to predict the spatially averaged hyporheic downwelling fluxes over the entire redd, $\bar{q}_d$, and over the portion that delivers oxygen-rich surface water to the egg pocket, $\bar{q}_{d,ep}$, (both normalized by the redd hydraulic conductivity (K) of the streambed sediment, $\bar{q}_d^* = \bar{q}_d/K$ and $\bar{q}_{d,ep}^* = \bar{q}_{d,ep}/K$) yields the same set of dimensionless independent variables. The dimensionless downwelling velocity, q_d^*, also allows comparison between the homogenous and categorical heterogeneous hydraulic conductivity cases. When homogeneous q_d^* are plotted against those of the heterogeneous cases and fall on a 1:1 line, the system behaves linearly and supports our hypothesis. In our analysis, we did not consider the alluvium depth a hindrance and thus we neglected it. We performed regression analysis to characterize the functional relationship between the dependent dimensionless variables and the set of independent dimensionless variables, e.g., $H^* = f(Re, Fr, A_R, A/Y_0)$. The simulations were split into two groups, one with 21 simulations to develop regression curves and the other with 27 simulations to validate the curves.

Table 4. Summary of surface flow characteristics and redd sizes with L, M, S, VS and ES identifying the large, medium, small, very small, and extremely small sizes of 3.9, 2.8, 1.82, 1 and 0.914 m wavelengths and with aspect ratios of 0.077, 0.139, 0.265, 0.139 and 0.15 respectively (Deverall et al., 1993; Evenson, 2001; Tonina & Buffington, 2009a). The 21 simulations utilized for validation from the independent set of calibration are marked with an asterisk (*) on the redd size. The data source for velocity-depth paired values are (Fehlman, 1985), (Deverall et al., 1993), Columbia River (Mueller, 2005) and Sacramento River (Data from NOAA, Andrew Pike, Winter-run Chinook salmon Lifecycle model project).

Run Number	Flow Depth (m)	Velocity (m/s)	Froude Number (Fr)	Reynolds Number (Re)	Redd Size	Source
1	0.25	0.15	0.10	37158	L*	Fehlman
2	0.25	0.29	0.19	72829	L*	Fehlman
3	0.38	0.58	0.30	218913	L, M*, S	Deverall
4	0.75	0.35	0.13	260729	L	Deverall
5	1.14	0.68	0.20	764308	L	Sacramento river
6	1.67	0.91	0.23	1514422	L	Sacramento river
7	1.94	0.40	0.09	761129	L*, M, S*	Sacramento river
8	2.06	1.12	0.25	2291632	L	Sacramento river
9	2.31	0.59	0.12	1351410	L, M*, S	Sacramento river
10	2.47	1.28	0.26	3140267	L	Sacramento river
11	2.88	0.91	0.17	2597395	L*, M, S*	Sacramento river
12	3.30	1.69	0.30	5539369	L	Sacramento river
13	3.47	1.27	0.22	4377164	L*	Sacramento river
14	3.92	1.49	0.24	5801389	L, M*, S	Sacramento river
15	4.04	1.90	0.30	7624205	L	Sacramento river
16	4.39	1.68	0.26	7325435	L	Sacramento river
17	4.73	2.03	0.30	9537110	L	Sacramento river
18	4.84	1.85	0.27	8893582	L	Sacramento river
19	5.22	2.00	0.28	10369555	L*, M, S*	Sacramento river
20	5.69	2.21	0.30	12490049	L	Sacramento river
21	6.51	2.60	0.33	16811790	L, M*, S	Sacramento river
22	7.03	2.87	0.35	20039960	L	Sacramento river
23	7.30	0.60	0.07	4350445	L	Columbia river
24	7.95	3.26	0.37	25742122	L*, M*, S	Sacramento river
25	0.1	0.15	0.15	14899	VS*	This study
26	0.1	0.3	0.3	29798	VS	This study
27	0.2	0.15	0.11	29798	VS*	This study
28	0.2	0.3	0.21	59595	VS	This study
29	0.27	0.16	0.10	44118	ES*	Fehlman
30	0.22	0.29	0.2	64715	ES*	Fehlman
31	0.32	0.36	0.2	114040	ES*	Fehlman
32	0.27	0.49	0.3	132272	ES*	Fehlman

7 RESULTS

7.1 Modeled surface flow

Both relative water surface elevation, WSE_R, (Figure 7a) and relative total head, H_R, (Figure 7b) over the redd depend on flow depth and velocity. For the same water depth, both WSE_R and H_R amplitudes increase with stream velocity (Figure 7, compare runs 1 and 2). However, when keeping the same velocity, the H_R amplitude tends to remain constant with increasing depth, whereas WSE_R amplitude decreases with increasing depth (circle and downward triangle, runs 6 and 11). The deepest and fastest flow (diamond, run 24) causes the largest H_R amplitude over the redd (Figure 7b). As observed for dune-like bedforms, discharge regulates the magnitude of the pressure amplitude, which increases with discharge, but the shape of the pressure distribution remains the same regardless of discharge. Unlike dunes, which have only one minimum and one maximum pressure, redds have two minima, one at the head of the pit and one at the crest, and two maxima, one near the middle of the tailspill, and the other downstream of the crest, where the redd ends at the undisturbed bed (Figure 7b). The lowest minimum near-bed pressure occurs at the crest of the redd, and the highest near-bed pressure occurs along the middle of the tailspill.

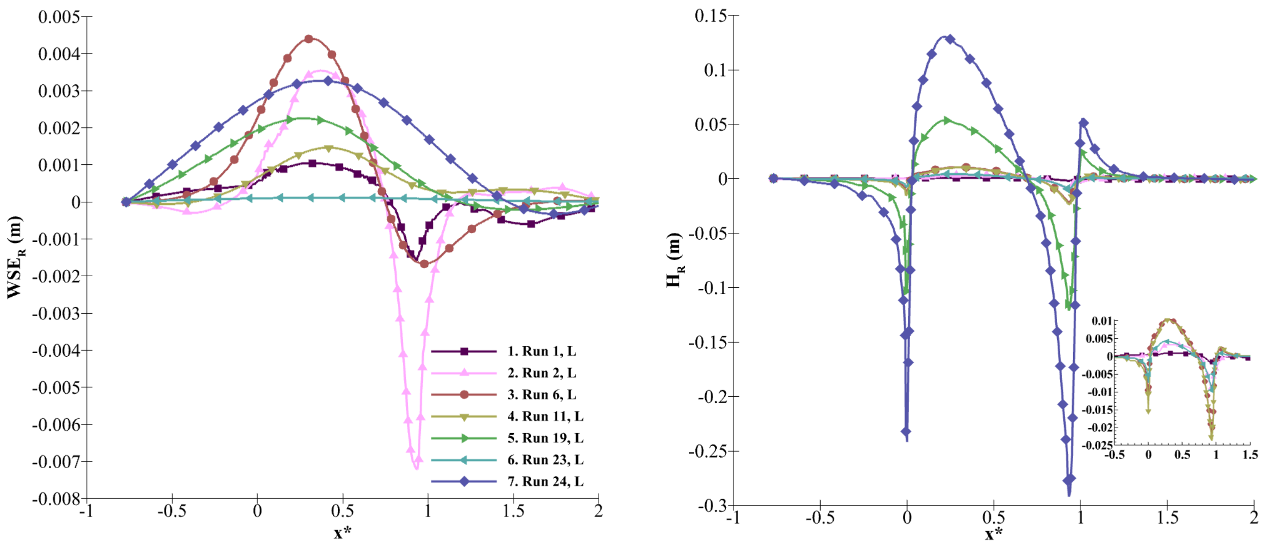

(a) (b)

Figure 7: (a) Relative water surface elevation (WSE_R) and (b) Relative total head (H_R) as a function of dimensionless distance x*, defined as the distance normalized by redd wavelength (x* = x/L), over the large redd size (3.9 m).

Redd aspect ratios affect the pressure drop magnitude, and large A_R values (~0.265) also have a profound impact on the shape of the pressure profile (Figure 8). The magnitude of the second maximum near-bed pressure value, which lies downstream of the crest, decreases as A_R increases until it disappears for A_R values between 0.14 and 0.26.

The interaction between surface flows and redd shapes and sizes (A_R) affect the flow velocity with stronger near-bed velocity gradients as either discharge or A_R increases (Figure 9). For each discharge and A_R, the highest velocity occurs on the crest of the redd, and the slowest velocity occurs in the pit. Another low velocity is detected just downstream of the redd's lee side. The size of the separation vortices within the pit increases as the surface flow velocity increases. The same is true with decreasing redd size, even for the same discharge. Another flow recirculation is developed just downstream of the tailspill for the smallest redd indicating that increasing discharges and A_R values result in increasing pressure amplitudes over the redd. This process causes a systematic increase of the total head drop, H^*, with an increase in the Reynolds, Froude, and A_R numbers (Figure 10).

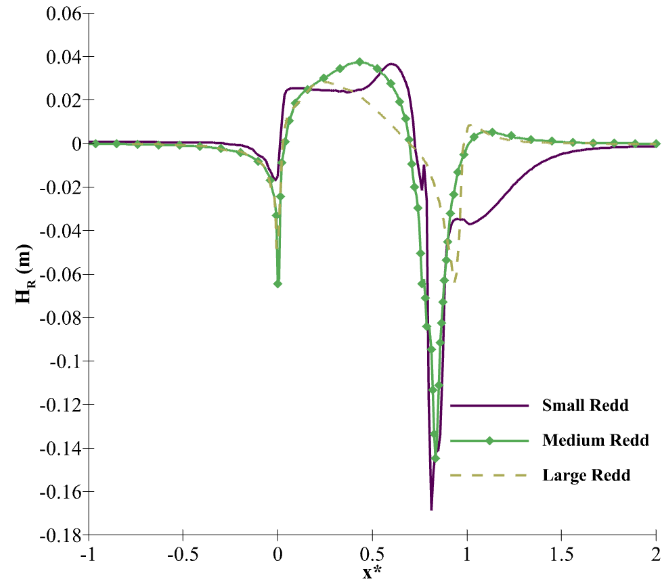

Figure 8: Relative total head (H_R) over three redd sizes (Small = 1.82 m, Medium = 2.8 m, and Large = 3.9 m) for Run 14. Aspect Ratios are A_R = 0.265, 0.139 and 0.077, respectively.

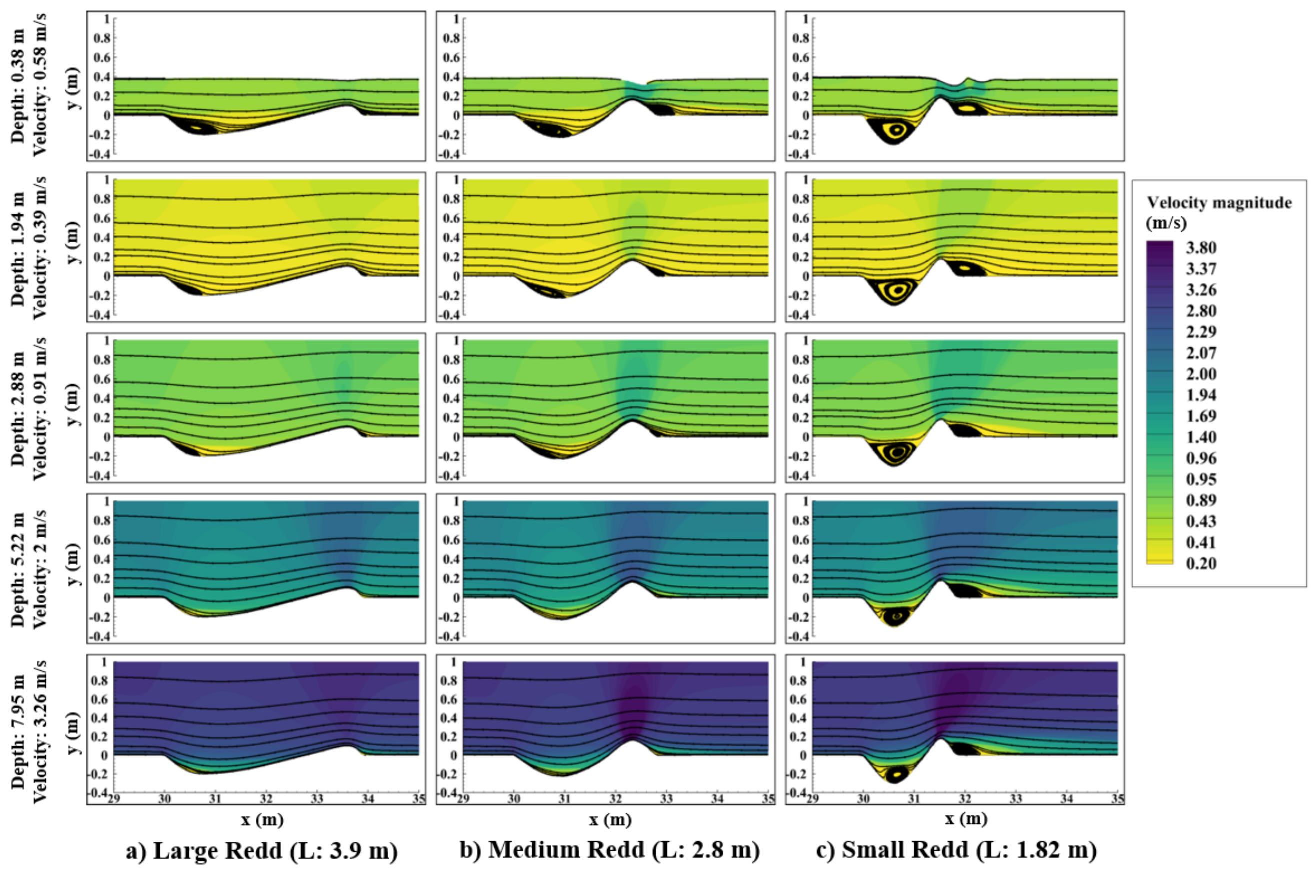

Figure 9: Surface flow characteristics for different surface hydrodynamics and different redd sizes.

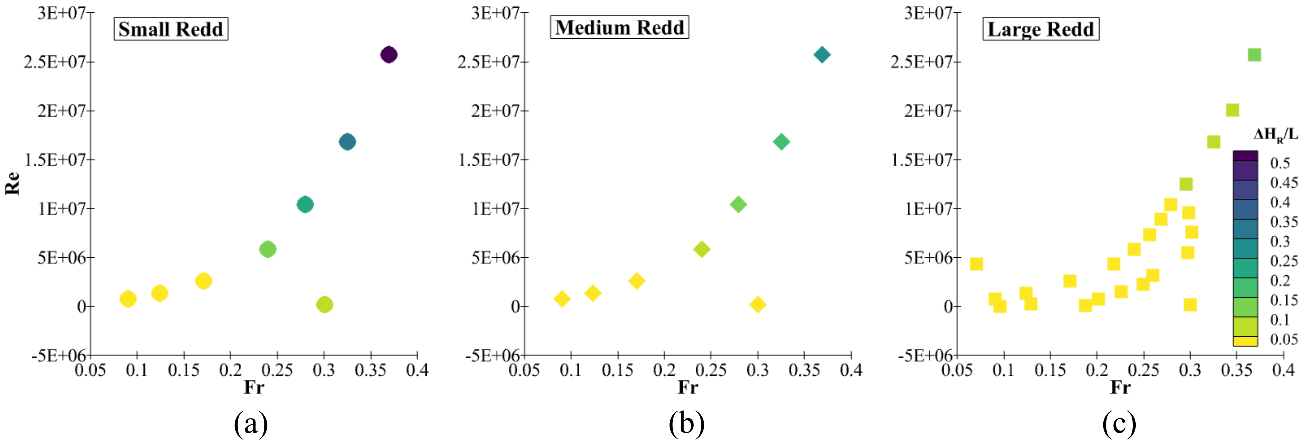

Figure 10: Dimensionless total head ($\Delta H_R/L$) as a function of Reynolds Number (*Re*), Froude Number (*Fr*), and Redd Aspect Ratio (A_R). Aspect Ratios are A_R = 0.265, 0.139, and 0.077 for small, medium, and large redd respectively.

7.2 Modeled hyporheic flow

Upwelling and downwelling fluxes, forming the hyporheic exchange, increase with discharge as seen in the increase in the normalized normal velocity distribution, $q^* = q / q_{max}$, defined as the normal velocity distribution (normal to the water bed surface) normalized by its maximum value, over the redd for different flow velocities and depths (Figure 11). q_{max} for small, medium and large redds are 0.00396 m/s, 0.0009 m/s and 0.00068 m/s, respectively. As with H_R, their magnitude decreases as water depth and velocity decrease. The highest redd aspect ratio gives rise to the maximum hyporheic exchange, the largest hyporheic cell size, and the highest downwelling velocity. High upwelling (negative normal velocity) and downwelling velocities are seen in the same locations as the high H_R values (compare Figure 7 and Figure 11). The surface flow-redd interaction formed three to four recirculating cells: one large cell with a downstream flow direction between the redd trough and crest, two with an upstream flow direction (one below the pit and one at the crest), and one slightly downstream of the crest (upstream flow direction) that did not appear for low A_R (Figure 12). The main hyporheic flow cell, which brings oxygen-rich surface water to the egg nest (see Figure 1 for potential locations of the egg pocket), has most of the flux upwelling at the crest's low-pressure zone, while a portion is entrained by the underflow and does not return to the river. Between slightly downstream of the pit and upstream of the tailspill of the redd, the flow reaches the egg pocket before arching back to the streambed surface. Both spatially averaged downwelling velocities ($\overline{q}_d$, and $\overline{q}_{d,ep}$) systematically increase with the larger Reynolds and Froude numbers, as well as redd A_R (Figure 13).

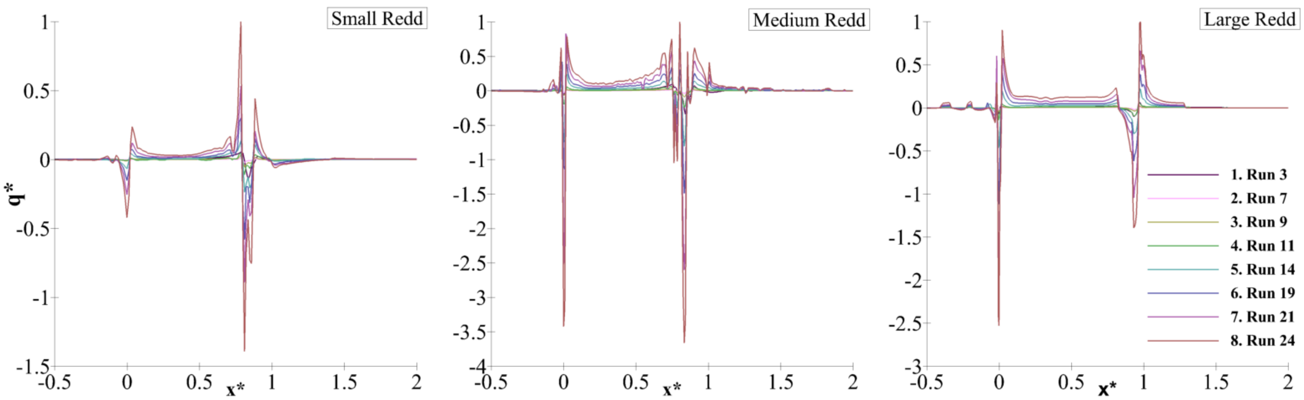

(a) (b) (c)

Figure 11: Normalized normal velocity distribution, $q^* = q / q_{max}$, (note y axes are not in the same scale to help visualize the lines), over a (a) small redd, (b) medium redd, and (c) large redd.

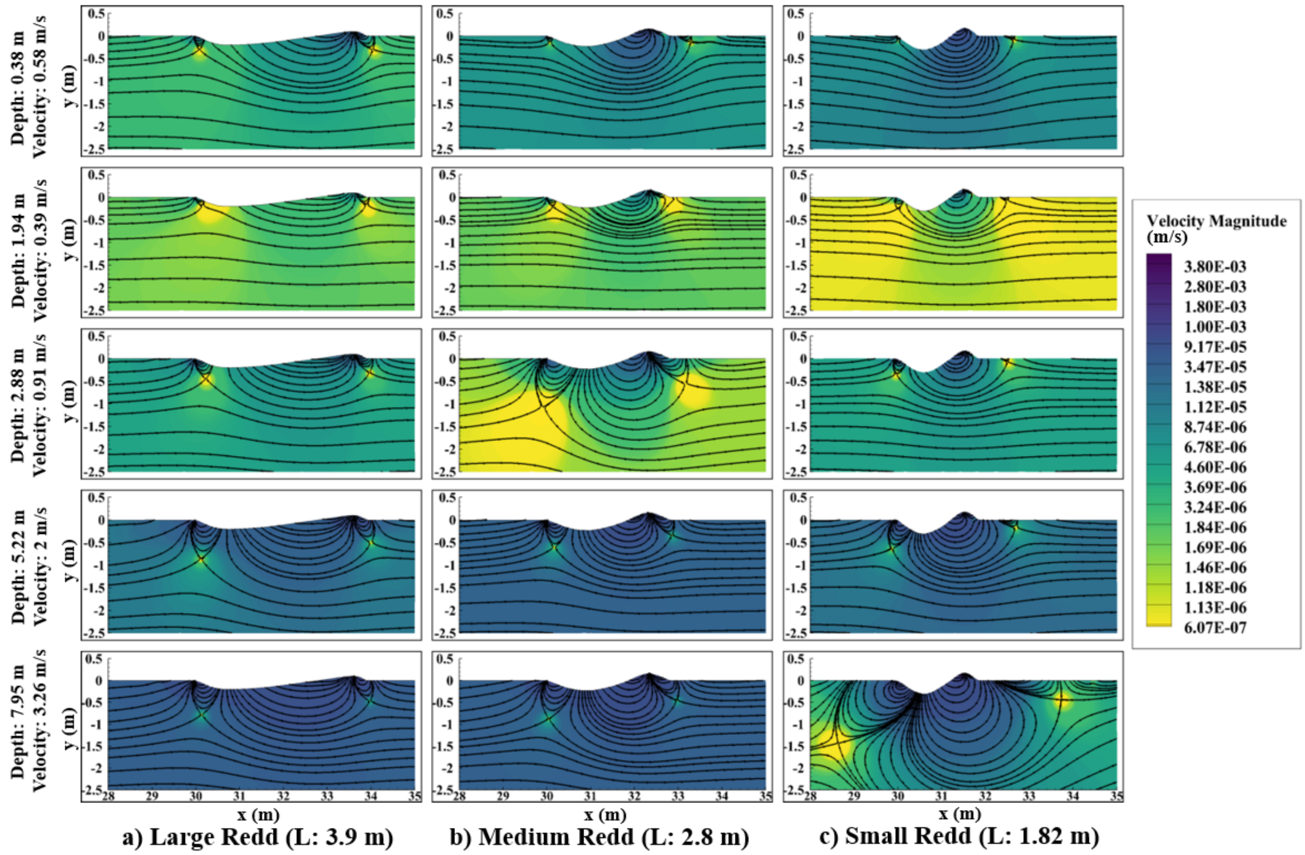

Figure 12: Subsurface flow characteristics for different surface hydrodynamics and three different redd sizes.

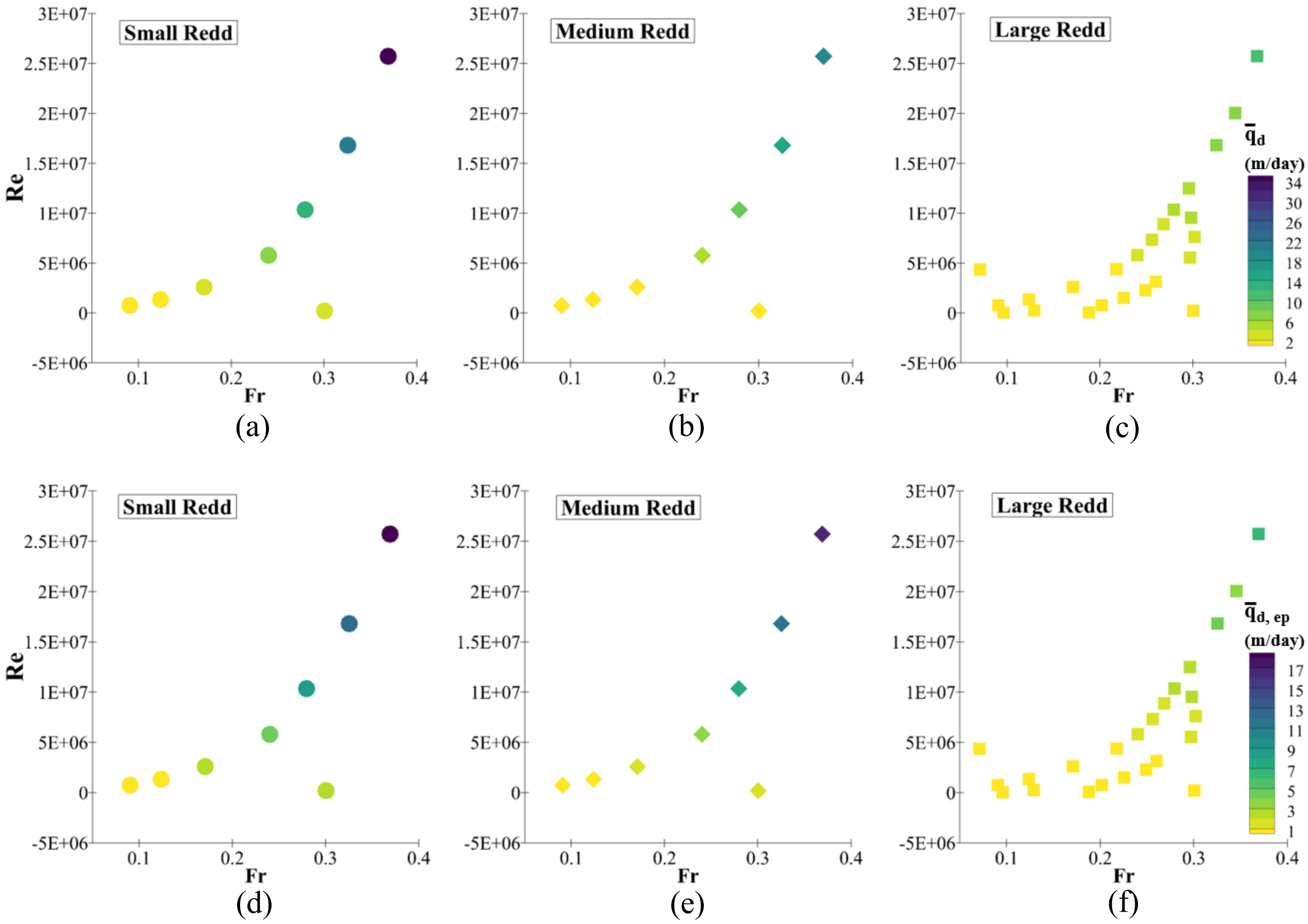

Figure 13: Averaged downwelling velocity over the redd ($\bar{q}_d$) (top panel) and between pit-tailspill region affecting the egg pocket ($\bar{q}_{d,ep}$) (bottom panel) as a function of Reynolds Number (Re), Froude Number (Fr), and Aspect Ratio (A_R).

7.3 Effect of categorical hydraulic conductivity

For Run 14 M (medium-sized redd), comparison of downwelling velocities between homogenous and categorical heterogeneous hydraulic conductivities with 5 and 10 times larger hydraulic conductivities in the redd than in the surrounding undisturbed sediment (Figure 14a) resulted in similar dimensionless downwelling velocities (Figure 14b). This shows that the redd hydraulic conductivity dominates the downwelling velocity and that the influence of heterogeneity between the redd and surrounding sediment is negligible on the flow field within the redd. Spatially averaged dowelling velocity over the redd and spatially averaged dowelling velocity going through the region of the egg pocket chiefly scale linearly with the hydraulic conductivity.

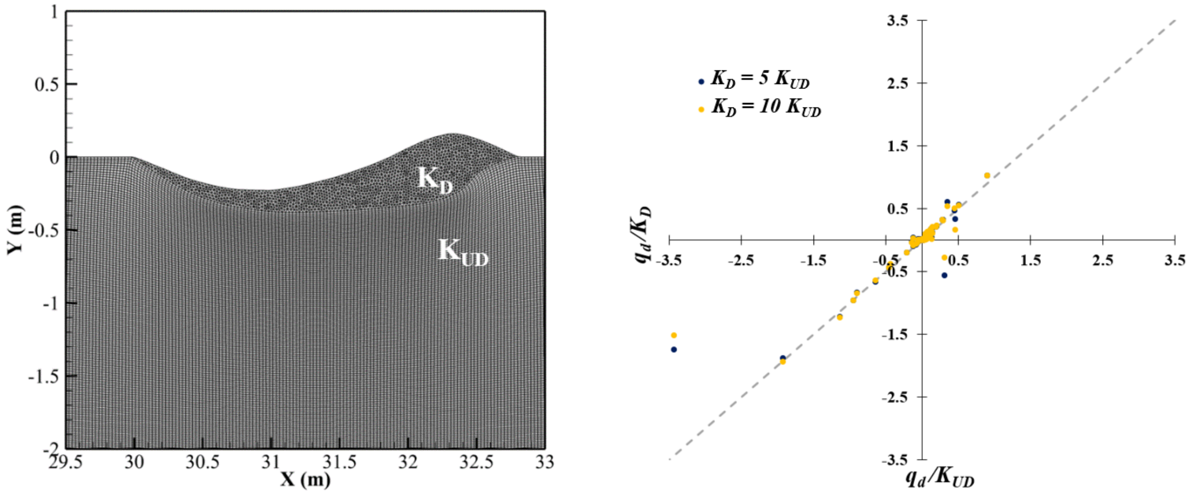

(a) (b)

Figure 14: (a) Redd disturbed and undisturbed sediment with their own hydraulic conductivities, K_D and K_{UD}, respectively. (b) Comparison between downwelling velocities normalized by the redd hydraulic conductivities for the homogeneous case (K_{UD}) and the heterogeneous (K_D) $K_D = 5 \cdot K_{UD}$ and $K_D = 10 \cdot K_{UD}$.

7.4 Regression predictive equations

The dimensional analysis was applied to the 3 dependent variables: total head drop (ΔH_R), downwelling velocity for the entire redd ($\bar{q}_d$), and downwelling velocity impacting only the egg pocket ($\bar{q}_{d,ep}$). Linear regression analysis of the log-transformed dimensionless numbers showed that *Fr* and *Re*, as well as A_R are statistically significant ($p < 0.01$), but the relative submergence was not ($p \sim 0.8$), on both total head drop and downwelling flux. Thus, it was eliminated from the regression analysis, resulting in three independent dimensionless quantities, *Fr*, *Re*, and A_R:

$$H^* = \frac{\Delta H_R}{L} = 0.122 \cdot (A_R)^{1.274} \cdot (Re)^{0.313} \cdot (Fr)^{2.219} \tag{4}$$

$$\bar{q}_d^* = \frac{\bar{q}_d}{K} = 0.052 \cdot (A_R)^{0.82} \cdot (Re)^{0.317} \cdot (Fr)^{1.91} \tag{5}$$

$$\bar{q}_{d,ep}^* = \frac{\bar{q}_{d.ep}}{K} = 0.112 \cdot (A_R)^{0.784} \cdot (Re)^{0.247} \cdot (Fr)^{1.91} \tag{6}$$

Comparisons of the model predictions against the independent data sets not used in the regression analysis showed very good performance with $R^2 > 0.9$ and strong correlations along the 1:1 line (Figure 15).

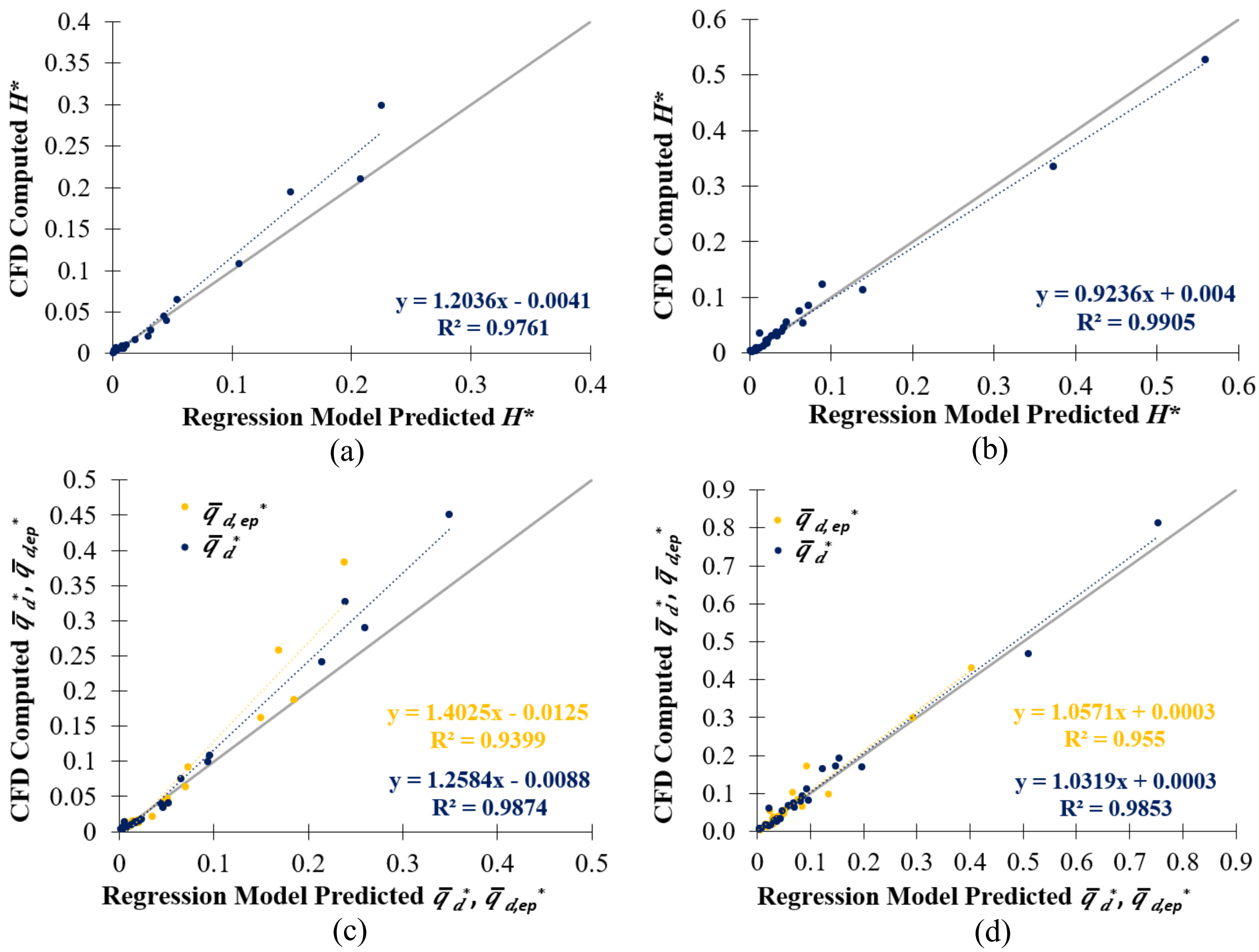

Figure 15: Linear regression plots for computed (y-axis) VS predicted (a) calibration and (b) validation of dimensionless total head drop across the redd. (c) Calibration and (d) validation of averaged downwelling velocities across the egg pocket (yellow) and entire redd (blue) for 48 runs (21 calibration and 27 validation).

We also tested whether equation (4) can predict the total head drop over dunes, extending the work of Fehlman (1985) (Figure 16a). The comparison shows a good fit ($R^2 \sim 0.9$), but model predictions are 2.5 times higher than those measured in Fehlman's experiments (Figure 16a). We ran a simulation with a sequence of redds and dunes for the flow conditions of Fehlman's (1985) run number 11 to test whether the presence of multiple redds would explain the difference. The three simulations (single redd, a sequence of 15 redds, and a sequence of 15 dunes) generated similar pressure distributions with the single redd having a slightly higher drop (Figure 16b). These results show that the difference is due to the shape of the dune rather than the fact that redds are typically isolated features, and dunes are a succession of bedforms adjacent to one another (Figure 16b).

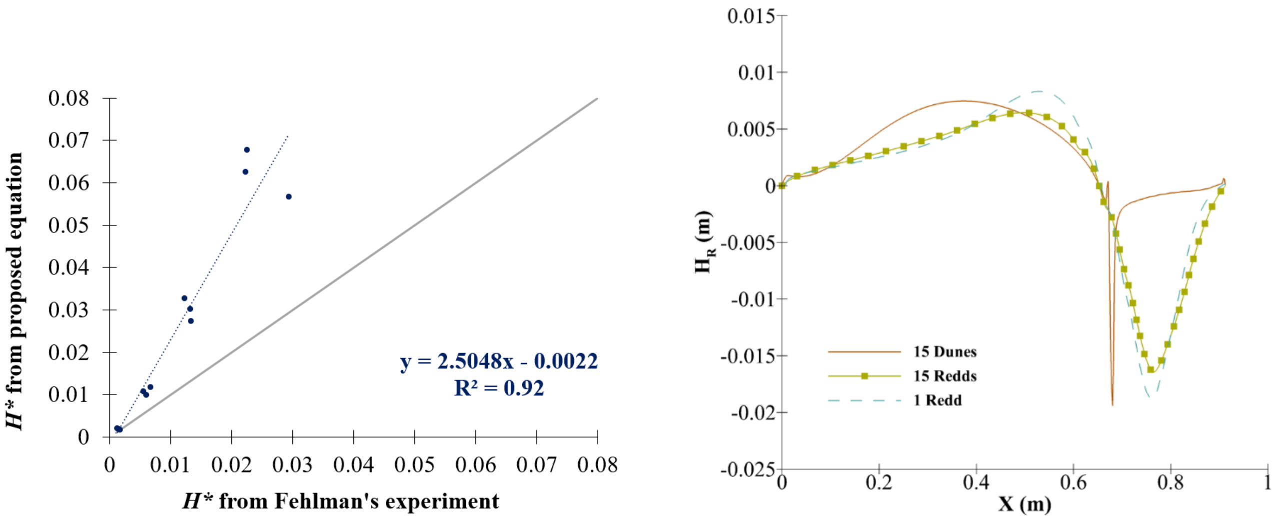

(a) (b)

Figure 16: (a) Total head drop normalized by the length of the dune (*ΔH_R/L*) across the uniform bedform for the flow hydraulics used in Fehlman's experiment for dunes using our proposed equation and (b) pressure distribution over a sequence of 15 dunes, a sequence of 15 redds, and one redd.

Note that the dramatic drop in relative head for the 15-dunes case, occurring around x = 0.7 m is due to the sharp edge at triangular dunes and a more appropriate minimum head value would be around -0.01 m rather than -0.02 H_R. This is a significant result because it implies that the proposed equation (4) can be extended to dunes by dividing H_R by a constant factor of 5 (2.5 times 2 where 2 accounts for semi-amplitude), resulting in semi-amplitude as given by equation (7) because Elliott and Brooks used semi-amplitude rather than amplitude:

$$h_{dune} = \frac{0.122}{5} \cdot \left(\frac{A}{L}\right)^{1.274} \cdot (Re)^{0.313} \cdot (Fr)^{2.219} \qquad (7)$$

where h_{dune} is the semi amplitude ($H^*/2$).

8 DISCUSSION

Our surface flow range is fairly extensive, encompassing spawning areas ranging from very shallow to very deep flows, as well as slow and fast water. Because the depth and velocity quantities are not independent as expressed through the resistance equation, e.g., Manning's equation, we did not keep one constant and change the other arbitrarily; instead, we modified them both simultaneously because an increase in discharge results in an increase in both velocity and depth. Our hydraulic scenarios also aim to replicate what is observed in the field in locations near redds. River management teams commonly use reach-averaged values, so the flow hydraulics used are reach-averaged values rather than local flow velocities and depths over a specific redd.

We employed a VOF model that allows tracking of the free surface elevation, which helps to better represent the pressure distribution at the water-sediment interface accurately. Most computational fluid dynamics models have used a single-phase with a rigid-lid approximation. However, we used a two-phase model (flow of the water column with air above it) because both hydrostatic and nonhydrostatic-driven fluxes can significantly increase when compared to the rigid-lid approach because we are analyzing surface flows within a wide range of Froude numbers (Lee et al., 2021), and the deformation of the river's free surface may influence to redd-driven hyporheic exchange. The fixed lid approach can be beneficial where no large changes in water surface elevations occur and where the VOF method may be computationally expensive.

Our numerical modeling demonstrates the impact of salmon redd shape and size, as well as surface discharge, on the hyporheic flow inside the redd, which directly influences the embryos. As seen in earlier publications (Stonedahl et al., 2010; Wörman et al., 2007), multiscale hyporheic flows are driven by the superposition of multiple scales of geomorphic features, and multi-cell hyporheic exchange is formed when surface flows interact with a redd (Tonina & Buffington, 2009a). The near-bed pressure distribution produces the largest flow circulation at the region between the redd pit bottom and the crest, where eggs incubate. Other secondary hyporheic exchange cells whose formation and relative size are dependent on flow hydraulics and redd aspect ratio, develop adjacent to the large flow circulation. This large hyporheic exchange cell is always present and has a downstream flow direction regardless of flow hydraulics or redd size, whereas the other smaller hyporheic exchange cells develop and grow with higher discharges and larger A_R values and can disappear with lower discharge and smaller A_R values. Another small cell is formed downstream of the tailspill for the highest A_R, which develops in size as the discharge increases. The large, constant cell, between the pit and the crest, is the most crucial for egg development as it supplies oxygen-rich surface water to the egg pocket. The generated downwelling flux increases with discharge and aspect ratio, suggesting that smaller redds with larger amplitudes may benefit from higher interstitial flows more than large redds with smaller amplitudes.

For a given redd configuration, larger discharges with the same water temperature will supply more oxygen-rich water to developing embryos as downwelling flux increases with discharge. This might have an important implication in managing water resources from dam releases or water diversion during the embryo's development. For oxygen delivery and consumption, however, both water temperature and interstitial flow velocity are important during embryos' development stage (Martin et al., 2020). In managed rivers such as the Sacramento River, high levels of water discharge can more rapidly deplete cool water pools stored in dams and thus lead to elevated temperature exposure during the embryonic period (Anderson et al., 2022). As a result, our findings should be interpreted in combination with a biophysical model of oxygen supply and demand for developing embryos to fully comprehend the significance of discharge for embryo survival (Martin et al., 2020).

When salmon spawn, they alter the morphology of the riverbed forming the typical dune-like redd and increase the redd hydraulic conductivity compared to the surrounding undisturbed sediment and thereby hyporheic exchange because spawning loosens the bed and washes particles from the gravels

(Chapman, 1988; Zimmermann & Lapointe, 2005a). This is beneficial to the embryos because this increases the advection of dissolved oxygen and nutrients from the stream to the egg pocket. Hydraulic conductivity in redds for chinook salmon was found to vary from $3\cdot10^{-2}$ m/s (Chapman et al., 1986) to $1.5\cdot10^{-4}$ m/s (Geist, 2005; Malcolm et al., 2004) in unspawned beds. Here we show the effect of categorical heterogeneity between a newly formed redd and undisturbed material that does not focus downwelling flow. The hyporheic flows within the egg pocket are dominated by the redd hydraulic conductivity regardless of the surrounding undisturbed condition. This result is supported by earlier simulations of Tonina & Buffington (2009b), although they did not report this behavior. This suggests that the reduction of the redd hydraulic properties over time from newly built redds toward undisturbed material (Zimmermann & Lapointe, 2005a, 2005b) can be studied by reducing the hydraulic conductivity of the homogeneous case. Thus, the advantage of the proposed normalization of the downwelling fluxes by the redd hydraulic conductivity (equations 5, 6) is that it allows the model to be applied to different permeabilities that may vary not only temporally but also among redds.

The size and shape of salmon redd varies enormously both within and across species (Deverall et al., 1993; Evenson, 2001; Tonina & Buffington, 2009a). However, the biological implications of this phenotypic variability for oxygen supply to developing embryos has been unknown. Here, for the first time, we quantified how redd size and shape influence interstitial flows within the redd. We found that the effect of redd morphology and stream discharge on interstitial flow can be characterized primarily by the aspect ratio of the redd, along with the Reynolds number and Froude number. We found that the Reynolds number, Froude number and aspect ratio significantly affect flow velocity within the redd using regression analysis, based on the subset of the 21 simulations that encompass the varied sizes of redd and surface discharge. The size of the redd, the velocity of the surface stream, and the depth of the flow are all represented by these variables. As *Re* increases, more pressure builds up on the redd, which is then modulated by the *Fr* and A_R, causing hyporheic flow to increase.

Flows across dunes, which have a similar form as redds, can be used to understand the influence of the redd aspect ratio on hyporheic flows. Larger head gradients and faster pore water velocities are produced by dunes with taller bedforms (Lee et al., 2020), just as they are found in our model for redds with larger aspect ratios. The total head drop found in our model, which is about twice as large as that reported in Fehlman's (1985) experiment (Figure 16), might be attributed to the shape of the redd with the pit and the hump (Figure 3 and Figure 7), while the impact of a single versus a sequence of features has negligible effect. This allows us to propose a new equation for semi-amplitude head drop around a dune bedform, which extends that of Elliott and Brooks (1997a) by accounting for the dune aspect ratio and Reynolds number whose effects were not accounted for because of the narrow range of hydraulic variability in Fehlman's (1985) experiments.

One of the limitations of our study's separate domain analysis approach is that the pressure profile obtained from the surface waterbed is used as the pressure inlet boundary condition for coupling the surface and subsurface domains. (Broecker et al., 2019) found that not only does surface water influence the subsurface, but the subsurface also influences the surface flow conditions. However, for the range of hydraulic conductivity we used, the exchange in mass between surface and subsurface is small and downwelling mass flux is less than 1% of the total mass transported by the surface flow.

9 CONCLUSION

Building on previous studies, we quantify the systematic change of hyporheic exchange induced by the redd-stream flow interaction for a broad range of surface flow hydraulics and redd sizes. Our simulations show that the total head gradient across the redd increases with the redd aspect ratio and river discharge. Regardless of surface flow hydraulics, the shape of the total head distribution over the redd stays typically similar, with the two lowest heads occurring at the beginning and crest of the redd and a high head in between the pit and the tailspill. Simulations show another high total head located on the streambed downstream of the redd, but its intensity decreases with redd aspect ratio and disappears for the smallest aspect ratio (0.077) studied here.

The highest hyporheic fluxes occur in the redd near the egg pocket. This suggests that, by the way in which they form their redds, salmonids actively enhance the environmental conditions of the egg habitat. The spawning activities alter both streambed morphology and sediment permeability, which after spawning activity, is higher in the redd than the surrounding sediment. The effect of altered hydraulic conductivity can be chiefly captured using the homogenous hydraulic conductivity of the disturbed sediment for the entire domain, e.g., redd and undisturbed material. This is because the redd-induced pressure profile mainly keeps the flow lines within the shallow near-surface domain of the disturbed sediment.

Based on dimensional analysis, our simulations allow identifying a set of regression equations, which predict the total head drop and the mean downwelling hyporheic fluxes from three dimensionless independent variables: the Reynolds number, the Froude number, and the redd aspect ratio. The regression equation for the mean downwelling velocity in the egg pocket could be used to quantify the hydraulic characteristics of the interstitial flows experienced by the egg and thus study an embryo's habitat. The regression equation for the total head amplitude extends the range of applicability of that proposed by Elliott and Brooks (1997b) based on Fehlman's (1985) dataset and thus provides an important tool to study hyporheic processes induced by dune-like bedforms.

Acknowledgement

This research has been supported by the grant 19-028-300 California State Water Resources Control Board. We would like to thank Andrew Pike who share the velocity-depth coupled at redd locations

along the Sacrament River quantified in the project Winter-run Chinook salmon Lifecycle model project. All data have been reported in the hydroshare repository Bhattarai et al (2022), http://www.hydroshare.org/resource/6deaf594de954b95b81bd117bd919960.

REFERENCES

Anderson, J. J., Beer, W. N., Israel, J. A., & Greene, S. (2022). Targeting river operations to the critical thermal window of fish incubation: Model and case study on Sacramento River winter-run Chinook salmon. *River Research and Applications*, *38*(5), 895–905. https://doi.org/10.1002/rra.3965

ANSYS Fluent Theory Guide. (2019). Retrieved from http://www.ansys.com

Bhattarai, B., D. Tonina, W. J. Reeder, R. Budwig, B. Hilliard, B. Martin, T. Xing (2022). Salmon Redd induced Hyporheic Flow, HydroShare, http://www.hydroshare.org/resource/6deaf594de954b95b81bd117bd919960

Bjornn, T. C., & Reiser, D. W. (1991). Habitat requirements of salmonids in streams. In W. R. Meehan (Ed.), *Influence of forest and rangeland management on salmonid fishes and their habitats* (pp. 83–138). Am. Fish. Soc. Spec. Publ. 19. Bethesda, Md.

Boano, F., Harvey, J. W., Marion, A., Packman, A. I., Revelli, R., Ridolfi, L., & Wörman, A. (2014). Hyporheic flow and transport processes: Mechanisms, models, and biogeochemical implications. *Reviews of Geophysics*, *52*(4), 603–679. https://doi.org/10.1002/2012RG000417

Boyd, J. W., Oldenburg, E. W., & Mcmichael, G. A. (2010). Color photographic index of fall chinook salmon embryonic development and accumulated thermal units. *PLoS ONE*, *5*(7). https://doi.org/10.1371/journal.pone.0011877

Broecker, T., Teuber, K., Gollo, V. S., Nützmann, G., Lewandowski, J., & Hinkelmann, R. (2019). Integral flow modelling approach for surface water-groundwater interactions along a rippled streambed. *Water (Switzerland)*, *11*(7). https://doi.org/10.3390/w11071517

Burner, C. J. (1951). Characteristics of spawning nests of Columbia River salmon. *Fishery Bulletin*, *52*, 97–110.

Buxton, T. H., Buffington, J. M., Tonina, D., Fremier, A. K., & Yager, E. M. (2015). Modeling the influence of salmon spawning on hyporheic exchange of marine-derived nutrients in gravel stream beds. *Canadian Journal of Fisheries and Aquatic Sciences*, *72*(8), 1146–1158. https://doi.org/10.1139/cjfas-2014-0413

Buxton, T. H., Buffington, J. M., Yager, E. M., Hassan, M. A., & Fremier, A. K. (2015). The relative stability of salmon redds and unspawned streambeds. *Water Resources Research*, *51*(8), 6074–6092. https://doi.org/10.1002/2015WR016908

Cardenas, Ford, A. E. A., Kaufman, M. H., Kessler, A. J., Cook, P. L. M., … M. K.-J. of, & 2016, U. (2016). Hyporheic flow and dissolved oxygen distribution in fish nests: The effects of open channel velocity, permeability patterns, and groundwater upwelling. *Journal of Geophysical Research: Biogeosciences*, *121*(12), 3113–3130. https://doi.org/10.1002/2016JG003381

Cardenas, M. B., & Wilson, J. L. (2007a). Dunes, turbulent eddies, and interfacial exchange with permeable sediments. *Water Resources Research*, *43*(8), 1–16. https://doi.org/10.1029/2006WR005787

Cardenas, M. B., & Wilson, J. L. (2007b). Exchange across a sediment–water interface with ambient groundwater discharge. *Journal of Hydrology*, *346*, 69–80.

Chapman, D. W. (1988). Critical review of variables used to define effects of fines in redds of large salmonids. *Transactions of the American Fisheries Society*, *117*(1), 1–21.

Chapman, D. W., Weitkamp, D. E., Welsh, T. L., Dell, M. B., & Schadt, T. H. (1986). Effects of River Flow on the Distribution of Chinook Salmon Redds. *Transactions of the American*

Fisheries Society, *115*(4), 537–547. https://doi.org/10.1577/1548-8659(1986)115<537:eorfot>2.0.co;2

Chen, X., Cardenas, M. B., & Chen, L. (2015). Three-dimensional versus two-dimensional bed form-induced hyporheic exchange. *Water Resources Research*, *51*, 2923–2936. https://doi.org/10.1002/ 2014WR016848

Coble, D. W. (1961). Influence of water exchange and dissolved oxygen in redds on survival of steelhead trout embryos. *Transactions of the American Fisheries Society*, *90*, 469–474.

Cooper, A. C. (1965). The effect of transported stream sediments on the survival of sockeye and pink salmon eggs and alevins. Int. Pac. *Salmon Fishery Commission Bulletin Bulletin*, (18), 18.

Crisp, D. T., & Carling, P. A. (1989). Observations on siting, dimensions, and structure of salmonid redds. *Journal of Fish Biology*, *34*, 119–134.

Deverall, K. R., Kelso, J. R. M., & James, G. D. (1993). Redd characteristics and implications for survival of chinook salmon (Oncorhynchus tshawytscha) embryos in the Waitaki river, New Zealand. *New Zealand Journal of Marine and Freshwater Research*, *27*(4), 437–444. https://doi.org/10.1080/00288330.1993.9516585

DeVries, P. (1997). Riverine salmonid egg burial depths: Review of published data and implications for scour studies. *Canadian Journal of Fisheries and Aquatic Sciences*, *54*(8), 1685–1698. https://doi.org/10.1139/f97-090

DeVries, P. (2012). Salmonid influences on rivers: A geomorphic fish tail. *Geomorphology*, *157–158*, 66–74. https://doi.org/10.1016/j.geomorph.2011.04.040

Elliott, A. H. (1990). *Transfer of solutes into and out of streambeds*. Pasadena, CA: WM Keck Laboratory of Hydraulics and Water Resources, Calif. Inst. of Technol.

Elliott, A. H., & Brooks, N. H. (1997a). Transfer of nonsorbing solutes to a streambed with bed forms: laboratory experiments. *Water Resources Research*, *33*(1), 137–151.

Elliott, A. H., & Brooks, N. H. (1997b). Transfer of nonsorbing solutes to a streambed with bed forms: Theory. *Water Resources Research*, *33*(1), 123–136. https://doi.org/10.1029/96WR02784

Evenson, D. F. (2001). *Egg pocket depth and particle size composition within Chinook salmon redds in the Trinity River, California*. Humboldt State University.

Fehlman, H. M. (1985). Resistance Components and Velocity Distributions of Open Channel Flows Over Bedforms.

Geist. (2005). A conceptual spawning habitat model to aid in ESA recovery plans for snake river fall chinook salmon. *BPA Report DOE/BP*, *00000652–2*(September), i–iii, 1–16.

Geist, & Dauble, D. D. (1998). Redd site selection and spawning habitat use by fall chinook salmon: The importance of geomorphic features in large rivers. *Environmental Management*, *22*(5), 655–669. https://doi.org/10.1007/s002679900137

Groot, C., & Margolis, L. (1991). *Pacific salmon life histories*. Vancouver, Canada: Columbia Press.

Hassan, M. A., Tonina, D., & Buxton, T. H. (2015). Does small-bodied salmon spawning activity enhance streambed mobility? *Water Resources Research*, *51*(9), 7467–7484. https://doi.org/10.1002/2015WR017079

Hendry, A. P., Morbey, Y. E., Berg, O. K., & Wenburg, J. K. (2004). Adaptive variation in senescence: Reproductive lifespan in a wild salmon population. *Proceedings of the Royal Society B: Biological Sciences*, *271*(1536), 259–266. https://doi.org/10.1098/rspb.2003.2600

Hirt, C. W., & Nichols, B. D. (1981). Volume of fluid (VOF) method for the dynamics of free boundaries. *Journal of Computational Physics*, *39*, 201–225.

Janssen, F., Cardenas, M. B., Sawyer, A. H., Dammrich, T., Krietsch, J., & De Beer, D. (2012). A comparative experimental and multiphysics computational fluid dynamics study of coupled surface-subsurface flow in bed forms. *Water Resources Research*, *48*(8), 1–16. https://doi.org/10.1029/2012WR011982

Lee, A., Aubeneau, A. F., & Cardenas, M. B. (2020). The Sensitivity of Hyporheic Exchange to Fractal Properties of Riverbeds. *Water Resources Research*, *56*(5), 1–15. https://doi.org/10.1029/2019WR026560

Lee, A., Aubeneau, A., Liu, X., & Cardenas, M. B. (2021). Hyporheic Exchange in Sand Dunes Under a Freely Deforming River Water Surface. *Water Resources Research*, *57*(3), 1–13. https://doi.org/10.1029/2020WR028817

Malcolm, I. A., Soulsby, C., Youngson, A. F., Hannah, D. M., McLaren, I. S., & Thorne, A. (2004). Hydrological influences on hyporheic water quality implications for salmon egg survival. *Hydrological Processes*, *18*(9), 1543–1560. https://doi.org/10.1002/hyp.1405

Martin, B. T., Pike, A., John, S. N., Hamda, N., Roberts, J., Lindley, S., & Danner, E. M. (2017). Phenomenological vs. biophysical models of thermal stress in aquatic eggs. *Ecology Letters*, *20*(1), 50–59.

Martin, B. T., Dudley, P. N., Kashef, N. S., Stafford, D. M., Reeder, W. J., Tonina, D., et al. (2020). The biophysical basis of thermal tolerance in fish eggs: Thermal tolerance in fish eggs. *Proceedings of the Royal Society B: Biological Sciences*, *287*(1937). https://doi.org/10.1098/rspb.2020.1550rspb20201550

Merz, J. E., Setka, J. D., Pasternack, G. B., & Wheaton, J. M. (2004). Predicting benefits of spawning-habitat rehabilitation to salmonid (Oncorhynchus spp.) fry production in a regulated California river. *Canadian Journal of Fisheries and Aquatic Sciences*, *61*(8), 1433–1446. https://doi.org/10.1139/F04-077

Meselhe, E. A., & Odgaard, A. J. (1998). 3D Numerical Flow Model for Fish Diversion Studies at Wanapum Dam. *Journal of Hydraulic Engineering*, *124*(12), 1203–1214.

https://doi.org/10.1061/(asce)0733-9429(1998)124:12(1203)

Monofy, A., & Boano, F. (2021). The Effect of Streamflow, Ambient Groundwater, and Sediment Anisotropy on Hyporheic Zone Characteristics in Alternate Bars. *Water Resources Research*, *57*(1), 1–22. https://doi.org/10.1029/2019WR025069

Monsalve, A., & Yager, E. M. (2017). Bed Surface Adjustments to Spatially Variable Flow in Low Relative Submergence Regimes. *Water Resources Research*, *53*(11), 9350–9367. https://doi.org/10.1002/2017WR020845

Moreto, J. R., Reeder, W. J., Budwig, R., Tonina, D., & Liu, X. (2022). Experimentally Mapping Water Surface Elevation, Velocity, and Pressure Fields of an Open Channel Flow Around a Stalk. *Geophysical Research Letters*, *49*(7), 1–10. https://doi.org/10.1029/2021gl096835

Moriasi, D. N., Arnold, J., Van Liew, M., Bingner, R., Harmel, D., & Veith, T. (2007). Model evaluation guidelines for systematic quantification of accuracy in watershed simulations. *Transactions of the American Society of Agricultural and Biological Engineers*, *50*(3), 885–900.

Mueller, R. (2005). *Deepwater Spawning of Fall Chinook Salmon (Oncorhynchus tshawytscha) near Ives and Pierce Island of the Columbia River, 2004-2005 Annual Report, Project No. 199900301*.

Reeder, W. J. J., Quick, A. M. A. M., Farrell, T. B. T. B., Benner, S. G. S. G., Feris, K. P. K. P., & Tonina, D. (2018). Spatial and Temporal Dynamics of Dissolved Oxygen Concentrations and Bioactivity in the Hyporheic Zone. *Water Resources Research*, *54*(3), 2112–2128. https://doi.org/10.1002/2017WR021388

Riebe, C. S., Sklar, L. S., Overstreet, B. T., & Wooster, J. K. (2014). Optimal reproduction in salmon spawning substrates linked to grain size and fish length. *Water Resources Research*, *50*(2), 898–918. https://doi.org/10.1002/2013WR014231

Stonedahl, S. H., Harvey, J. W., Wörman, A., Salehin, M., & Packman, A. I. (2010). A multiscale model for integrating hyporheic exchange from ripples to meanders. *Water Resources Research*, *46*(12), 1–14. https://doi.org/10.1029/2009WR008865

Stuart, T. A. (1953a). *Spawning migration, reproduction and young stage of loch trout (Salmo trutta L.)*. *Freshwater and Salmon Fisheries Research*. Edinburgh, Scotland: Department of Agriculture and Fisheries.

Stuart, T. A. (1953b). Water currents through permeable gravel and their significance to spawning salmonids, etc. *Nature*, *172*, 407–408.

Tappel, P. D., & Bjornn, T. C. (1983). A New Method of Relating Size of Spawning Gravel to Salmonid Embryo Survival. *North American Journal of Fisheries Management*, *3*(2), 123–135. https://doi.org/10.1577/1548-8659(1983)3<123:anmors>2.0.co;2

Tonina, D., & Buffington, J. M. (2009a). A three-dimensional model for analyzing the effects of salmon redds on hyporheic exchange and egg pocket habitat. *Canadian Journal of Fisheries and Aquatic Sciences*, *66*(12), 2157–2173. https://doi.org/10.1139/F09-146

Tonina, D., & Buffington, J. M. (2009b). Hyporheic exchange in mountain rivers I: Mechanics and environmental effects. *Geography Compass*, *3*(3), 1063–1086. https://doi.org/10.1111/j.1749-8198.2009.00226.x

Trauth, N., Schmidt, C., Maier, U., Vieweg, M., & Fleckenstein, J. H. (2013). Coupled 3-D stream flow and hyporheic flow model under varying stream and ambient groundwater flow conditions in a pool-riffle system. *Water Resources Research*, *49*(9), 5834–5850. https://doi.org/10.1002/wrcr.20442

Wilson, R. V., Stern, F., Coleman, H. W., & Paterson, E. G. (2001). Comprehensive approach to verification and validation of CFD simulations—Part 2: Application for rans simulation of a cargo/container ship. *Journal of Fluids Engineering, Transactions of the ASME*, *123*(4), 803–

810. https://doi.org/10.1115/1.1412236

Wörman, A., Packman, A. I., Marklund, L., Harvey, J. W., & Stone, S. H. (2007). Fractal topography and subsurface water flows from fluvial bedforms to the continental shield. *Geophysical Research Letters*, *34*(7), 1–5. https://doi.org/10.1029/2007GL029426

Xing, T., & Stern, F. (2010). Factors of safety for Richardson extrapolation. *Journal of Fluids Engineering, Transactions of the ASME*, *132*(6), 0614031–0640313. https://doi.org/10.1115/1.4001771

Xing, T., & Stern, F. (2011). Closure to "discussion of 'factors of safety for Richardson Extrapolation'" (2011, ASME J. Fluids Eng., 133, p. 115501). *Journal of Fluids Engineering, Transactions of the ASME*, *133*(11), 2–7. https://doi.org/10.1115/1.4005030

Xing, T., Carrica, P., & Stern, F. (2008). Computational towing tank procedures for single run curves of resistance and propulsion. *Journal of Fluids Engineering, Transactions of the ASME*, *130*(10), 1011021–10110214. https://doi.org/10.1115/1.2969649

Yates, D., Galbraith, H., Purkey, D., Huber-Lee, A., Sieber, J., West, J., et al. (2008). Climate warming, water storage, and Chinook salmon in California's Sacramento Valley. *Climatic Change*, *91*(3–4), 335–350. https://doi.org/10.1007/s10584-008-9427-8

Zimmermann, A. E., & Lapointe, M. (2005a). Intergranular flow velocity through salmonid redds: Sensitivity to fines infiltration from low intensity sediment transport events. *River Research and Applications*, *21*(8), 865–881. https://doi.org/10.1002/rra.856

Zimmermann, A. E., & Lapointe, M. F. (2005b). Sediment infiltration traps: Their use to monitor salmonid spawning habitat in headwater tributaries of the Cascapédia River, Québec. *Hydrological Processes*, *19*(20), 4161–4177. https://doi.org/10.1002/hyp.5879